bioRxiv preprint doi: https://doi.org/10.1101/796581; this version posted January 30, 2020. The copyright holder for this preprint (which was not certified by peer review) is the author/funder, who has granted bioRxiv a license to display the preprint in perpetuity. It is made available under aCC-BY-NC 4.0 International license.

1 **Human iPSC modeling reveals mutation-specific responses to gene therapy in Best disease**

2

3 Divya Sinha[a,b,1], Benjamin Steyer[a,c,1], Pawan K. Shahi[a,d], Katherine Mueller[c], Rasa Valiauga[b], Kimberly
4 L. Edwards[b], Cole Bacig[b], Stephanie S. Steltzer[c], Sandhya Srinivasan[c], Amr Abdeen[c], Evan Cory[c],
5 Viswesh Periyasamy[c], Alireza Fotuhi Siahpirani[c], Edwin M. Stone[e], Budd A Tucker[e], Sushmita Roy[c,f],
6 Bikash R. Pattnaik[a,d,g,2], Krishanu Saha[a,c,h,2], David M. Gamm[a,b,g,2,3]

7 [a]McPherson Eye Research Institute, University of Wisconsin-Madison, Madison, WI, USA 53705

8 [b]Waisman Center, University of Wisconsin-Madison, Madison, WI, USA 53705

9 [c]Wisconsin Institute for Discovery, University of Wisconsin-Madison, Madison, WI, USA 53715

10 [d]Department of Pediatrics, University of Wisconsin-Madison, Madison, WI, USA 53792

11 [e]Department of Ophthalmology and Visual Sciences, Carver College of Medicine, Iowa City, IA 52242

12 [f]Department of Biostatistics, University of Wisconsin-Madison, Madison, WI, USA 53792

13 [g]Department of Ophthalmology and Visual Sciences, University of Wisconsin-Madison, Madison, WI,
14 USA 53705

15 [h]Department of Biomedical Engineering, University of Wisconsin-Madison, Madison, WI, USA 53706

16 [1]These authors contributed equally to the work

17 [2]**Co-Correspondence:**

18 **David M. Gamm**

19 1500 Highland Avenue, Madison, WI, USA 53705

20 E-mail: dgamm@wisc.edu; Phone: 608-261-1516

21 **Krishanu Saha**

22 330 N. Orchard Street,

23 Madison WI, USA 53715

bioRxiv preprint doi: https://doi.org/10.1101/796581; this version posted January 30, 2020. The copyright holder for this preprint (which was not certified by peer review) is the author/funder, who has granted bioRxiv a license to display the preprint in perpetuity. It is made available under aCC-BY-NC 4.0 International license.

24 E-mail: ksaha@wisc.edu; Phone: 608-316-4313

25 **Bikash R. Pattnaik**

26 1300 University Avenue, Madison, WI, USA 53706

27 E-mail: pattnaik@wisc.edu; Phone: 608-265-9486

28

29 [3]**Lead contact:** David M. Gamm

30 **Keywords:** human pluripotent stem cells, gene therapy, gene augmentation, autosomal dominant disease,

31 macular degeneration, orphan disease, channelopathy, somatic cell gene editing, CRISPR-Cas9

32

33 **Abstract:** Dominantly inherited disorders are not typically considered therapeutic candidates for gene

34 augmentation. Here, we utilized patient-specific induced pluripotent stem cell-derived retinal pigment

35 epithelium (iPSC-RPE) to test the potential of gene augmentation to treat Best disease, a dominant

36 macular dystrophy caused by over 200 missense mutations in *BEST1*. Gene augmentation in iPSC-RPE

37 fully restored BEST1 calcium-activated chloride channel activity and improved rhodopsin degradation in

38 iPSC-RPE models of recessive bestrophinopathy and dominant Best disease caused by two different ion

39 binding domain mutations. A dominant Best disease iPSC-RPE model that did not respond to gene

40 augmentation showed normalization of BEST1 channel activity following CRISPR-Cas9 editing of the

41 mutant allele. We then tested gene editing in all three dominant Best disease iPSC-RPE models, which

42 produced premature stop codons exclusively within the mutant *BEST1* alleles. Single-cell profiling

43 demonstrated no adverse perturbation of RPE transcriptional programs in any model, although off-target

44 analysis detected a silent genomic alteration in one model. These results suggest that gene augmentation is

45 a viable first-line approach for some dominant Best disease patients and that non-responders are

46 candidates for alternate approaches such as genome editing. However, testing genome editing strategies

bioRxiv preprint doi: https://doi.org/10.1101/796581; this version posted January 30, 2020. The copyright holder for this preprint (which was not certified by peer review) is the author/funder, who has granted bioRxiv a license to display the preprint in perpetuity. It is made available under aCC-BY-NC 4.0 International license.

47 for on-target efficiency and off-target events using patient-matched iPSC-RPE model systems is
48 warranted. In summary, personalized iPSC-RPE models can be used to select among a growing list of
49 gene therapy options to maximize safety and efficacy while minimizing time and cost. Similar scenarios
50 likely exist for other genotypically diverse channelopathies, expanding the therapeutic landscape for
51 affected patients.
52
53 **Significance**: Dominantly inherited disorders pose distinct challenges for gene therapies, particularly in
54 the face of extreme mutational diversity. We tested whether a broad gene replacement strategy could
55 reverse the cellular phenotype of Best disease, a dominant blinding condition that targets retinal pigment
56 epithelium (RPE). Using RPE generated from patient-specific induced pluripotent stem cells (iPSCs), we
57 show that gene replacement functionally overcomes some, but not all, of the tested mutations. In
58 comparison, all dominant Best disease models tested were phenotypically corrected after mutation-
59 specific genome editing, although one off-target genomic alteration was discovered. Our results support a
60 two-tiered approach to gene therapy for Best disease, guided by safety and efficacy testing in iPSC-RPE
61 models to maximize personal and public health value.
62
63
64 **Introduction:** Genotypically heterogeneous dominant diseases pose significant challenges and
65 opportunities for precision medicine (1). Among gene therapies, gene augmentation for recessive
66 disorders is the most developed, having spurred multiple clinical trials (2-4) and FDA approval for one
67 ocular disease (5). However, gene augmentation is generally ruled out as a stand-alone therapy for
68 dominant disorders due to a perceived need to eliminate the deleterious effects of the mutant allele. Gene
69 editing approaches to silence or repair mutant alleles hold promise in this regard (6-8), but testing safety
70 and efficacy for every mutant allele-specific genome editor presents practical and economic challenges in

bioRxiv preprint doi: https://doi.org/10.1101/796581; this version posted January 30, 2020. The copyright holder for this preprint (which was not certified by peer review) is the author/funder, who has granted bioRxiv a license to display the preprint in perpetuity. It is made available under aCC-BY-NC 4.0 International license.

71 diseases with high mutational diversity. Further, gene editing may not be able to target all mutations (6, 9,
72 10) and could lead to off-target mutagenesis—particularly within a heterozygous wildtype allele—or
73 other adverse events (11). Another consideration for gene therapy development is the need for preclinical
74 model systems with phenotypes and/or genotypes that are relevant to the human disease. This requirement
75 is particularly challenging for genome editing strategies, which utilize sequence-specific tools and thus
76 require human model systems to test safety and efficacy (12). Humanized animal models have also been
77 employed for this purpose (13), although they cannot be used for genome-wide off-target analysis.

78 One disorder that faces a full array of these therapeutic obstacles is Best disease, a major cause of
79 inherited macular degeneration that currently has no treatment options. Best disease exclusively targets
80 the retinal pigment epithelium (RPE), a monolayer of cells essential for the survival and function of
81 photoreceptors. Although Best disease is often diagnosed in early childhood based on its distinctive
82 ophthalmological findings (14), its effects on central vision are generally mild at first. Vision loss occurs
83 progressively and irreversibly over several decades, thus providing a wide time window for therapeutic
84 intervention.

85 Best disease is a genotypically diverse disorder transmitted primarily in an autosomal dominant
86 fashion, although rare cases of autosomal recessive bestrophinopathy (ARB) are known (15). Together,
87 autosomal dominant Best disease (adBD) and ARB are linked to over 200 mutations in the *BEST1* gene,
88 which encodes a putative homo-pentameric calcium-activated chloride channel (CaCC) found in the RPE.
89 Recent elucidation of the high-resolution crystal structure of chicken Best1 reinforced its role as a CaCC
90 and revealed that disease-associated mutations cluster within calcium or chloride ion binding sites or
91 within structural regions of the channel (16).

92 A significant impediment to the development of therapies for adBD is the lack of model systems
93 that adequately mimic the genotypic and phenotypic characteristics of the disorder. While canine models

bioRxiv preprint doi: https://doi.org/10.1101/796581; this version posted January 30, 2020. The copyright holder for this preprint (which was not certified by peer review) is the author/funder, who has granted bioRxiv a license to display the preprint in perpetuity. It is made available under aCC-BY-NC 4.0 International license.

94 of ARB mirror the human ARB phenotype (14), no suitable animal models of adBD exist. To provide a
95 therapeutic testing platform for adBD, we previously developed the first human iPSC-RPE models of the
96 disease, which demonstrated relevant cellular dysfunction; most notably, delayed degradation of
97 phagocytosed photoreceptor outer segment (POS) proteins (17, 18). These adBD iPSC-RPE models were
98 then used to test the potential for selected pharmacological interventions to ameliorate the cellular
99 phenotype of this disorder (18).

100 In the present study, we examined whether gene therapy could definitively correct the functional
101 defects present in adBD iPSC-RPE. Given that BEST1 forms a homo-pentameric CaCC, we hypothesized
102 that gene augmentation could potentially mitigate the cellular disease phenotype in adBD by increasing
103 the ratio of wild-type to mutant BEST1 monomers available for channel assembly. This theory presumes
104 that the deleterious effects of the mutant allele can be diluted sufficiently to restore CaCC function,
105 preferably in a controlled manner without the risks associated with unregulated transgene expression.

106 To test our hypothesis, we employed three iPSC-RPE models of adBD, along with one iPSC-RPE
107 model of ARB as a control. Importantly, the iPSC lines were generated from patients with *BEST1*
108 mutations in different functional regions of the channel (*i.e.*, calcium binding, chloride binding, and
109 structural) (16). We then ectopically expressed wildtype *BEST1* in iPSC-RPE using a viral vector that
110 incorporated the native *BEST1* promoter, *VMD2*, in order to maintain RPE specificity and to keep
111 transgene expression levels in check. Using this strategy, we obtained a >3-fold increase in wildtype
112 BEST1 protein expression across all adBD iPSC-RPE models. Single cell electrophysiology and cell
113 population-based assays revealed that two of the adBD mutations were exceedingly responsive to gene
114 augmentation alone. Indeed, the correction of the cellular disease phenotype observed in these adBD
115 iPSC-RPE models following gene augmentation was on par with that seen in the ARB iPSC-RPE model.

bioRxiv preprint doi: https://doi.org/10.1101/796581; this version posted January 30, 2020. The copyright holder for this preprint (which was not certified by peer review) is the author/funder, who has granted bioRxiv a license to display the preprint in perpetuity. It is made available under aCC-BY-NC 4.0 International license.

116 To address the adBD mutation that failed to respond to gene augmentation, as well as others that
117 may also be refractory to this broad therapeutic strategy, we examined whether CRISPR-Cas9 gene
118 editing could specifically target the mutant *BEST1* allele, leaving the normal allele intact. We found that
119 gene editing was highly efficient at eliminating mutant allele expression and restoring iPSC-RPE CaCC
120 activity in all three adBD models. These results bode well for the use of CRISPR-Cas9 to treat adBD
121 mutations that are not candidates for gene augmentation, contingent on the availability of suitable guide
122 RNAs. We then investigated whether gene editing caused untoward effects on the RPE transcriptome or
123 induced off-target genome alterations in any of the adBD models. While no transcriptomic perturbations
124 were detected, a single significant—albeit functionally silent—off-target site contained genomic
125 insertions and deletion mutations (indels) in one adBD model. Based on our findings, we propose a two-
126 tiered approach to adBD gene therapy that uses iPSC-RPE testing to first determine which mutations are
127 likely to respond to frontline treatment with gene augmentation. *BEST1* mutant iPSC-RPE models that do
128 not demonstrate phenotypic correction with gene augmentation would then undergo next-level safety and
129 efficacy testing to assess candidacy for customized genome editing.
130
131 **Results**
132 **BEST1 mutations decrease CaCC activity in patient-specific iPSC-RPE.**
133 In addition to the N926H and A146K adBD iPSC lines previously reported (17, 18), we generated
134 iPSCs from a third adBD patient with an R218C mutation and an ARB patient with compound
135 heterozygous mutations (R141H/A195V) (**Figure 1A**). Based on the crystallographic studies, each of
136 these mutations lies within a different functional region of the BEST1 channel (**Figure 1B**) (16). We also
137 employed two control iPSC lines: a wildtype (WT) iPSC line and an isogenic iPSC line generated via
138 CRISPR-based gene correction of R218C adBD iPSCs (R218C>WT) (19). All six iPSC lines were tested

bioRxiv preprint doi: https://doi.org/10.1101/796581; this version posted January 30, 2020. The copyright holder for this preprint (which was not certified by peer review) is the author/funder, who has granted bioRxiv a license to display the preprint in perpetuity. It is made available under aCC-BY-NC 4.0 International license.

139 for pluripotency, differentiated to RPE, and characterized (**Figures 1C-D, and S1A-D**). iPSC-RPE
140 monolayers for all adBD and control lines, but not the ARB line, showed robust levels of BEST1 protein
141 expression (**Figure 1D**). The profoundly decreased BEST1 level in our ARB cultures is consistent with
142 reports using heterologous expression or iPSC-RPE systems that showed low or undetectable levels of
143 R141H or A195V BEST1 (20, 21). As a measurement of CaCC activity, single-cell patch-clamp
144 recordings of calcium-activated chloride current density were performed and found to be greatly
145 diminished in all patient-specific iPSC-RPE relative to WT control iPSC-RPE (**Figures 1E and S1E-I**).
146 Gene-corrected R218C>WT isogenic iPSC-RPE control showed CaCC current density at levels similar to
147 native WT control lines (**Figures 1E and S1J**), indicating that the decreased CaCC activity was indeed
148 the result of the BEST1 mutation.
149

150 ***BEST1* augmentation restores CaCC activity and enhances rhodopsin degradation in ARB iPSC-**
151 **RPE.**

152 We next sought to confirm that ectopic expression of WT human BEST1 (hBEST1) could
153 ameliorate the disease phenotype of R141H/A195V ARB iPSC-RPE, analogous to gene augmentation
154 studies using ARB canines or other iPSC-RPE model systems for ARB (22, 23). Single-cell patch clamp
155 recordings of calcium-activated chloride current density were used as a readout of efficacy in iPSC-RPE
156 cells. In addition, we monitored degradation of rhodopsin following POS feeding as an assay of intact
157 RPE monolayer function.

158 For gene augmentation we used a lentivirus construct (*hVMD2-hBEST1-T2A-GFP*) designed to
159 co-express hBEST1 and green fluorescent protein (GFP) under control of the human *BEST1* promoter
160 (*hVMD2*), which assures both RPE-specific expression and *BEST1*-specific gene regulation (**Figures 2A,**
161 **B**). Lentivirus was chosen for transgene delivery based on its safe use in human retinal gene therapy trials

bioRxiv preprint doi: https://doi.org/10.1101/796581; this version posted January 30, 2020. The copyright holder for this preprint (which was not certified by peer review) is the author/funder, who has granted bioRxiv a license to display the preprint in perpetuity. It is made available under aCC-BY-NC 4.0 International license.

162 (24) (ClinicalTrials.gov Identifiers: NCT01367444, NCT01736592) and its superior transduction
163 efficiency in cultured human RPE (17, 25). GFP expression was observed in ARB iPSC-RPE cells post-
164 transduction, and immunocytochemical (ICC) and western blot analysis confirmed enhanced expression
165 of BEST1 in treated cultures (**Figures 2C, S2A-C**). By ≥4 weeks post-transduction, CaCC current density
166 in ARB iPSC-RPE increased significantly, reaching levels comparable to WT iPSC-RPE (**Figures 2D, E**
167 **and S2E**). Furthermore, transduced monolayers of ARB iPSC-RPE demonstrated enhanced degradation
168 of rhodopsin following POS feeding (**Figure 2F and S2I**). These findings, together with those reported
169 by Guziewicz et al. (22) and Li et al. (23), support *hBEST1* gene augmentation as a treatment for ARB.
170

171 ***BEST1* augmentation restores CaCC activity and enhances rhodopsin degradation in R218C and**
172 **N296H adBD iPSC-RPE, but not in A146K adBD iPSC-RPE.**

173 Although not as intuitive, we suspected that gene augmentation might also be a viable solo
174 therapeutic strategy for adBD-causing *BEST1* mutations. More specifically, we hypothesized that CaCC
175 activity could be restored by increasing the intracellular ratio of wildtype to mutant BEST1 monomers
176 available to form the homo-pentameric channel.

177 The same *hVMD2-hBEST1-T2A-GFP* lentiviral construct that was tested in ARB iPSC-RPE was
178 used to transduce iPSC-RPE from all three adBD patients (**Figure S2D**). Following gene augmentation,
179 BEST1 levels in each adBD iPSC-RPE model were comparable to those achieved in gene augmented
180 ARB-iPSC-RPE and >3-fold higher than BEST1 levels present in parallel cultures of untreated adBD
181 iPSC-RPE (**Figure 3A and S2C**). At ≥4 weeks post-transduction, CaCC activity was fully restored in the
182 R218C and N296H adBD iPSC-RPE models, whereas the A146K adBD iPSC-RPE model remained
183 unresponsive (**Figure 3B-D and S2F-H**) despite displaying the highest fold increase in BEST1
184 expression (**Figure 3A**). Consistent with these single-cell electrophysiological findings, gene

bioRxiv preprint doi: https://doi.org/10.1101/796581; this version posted January 30, 2020. The copyright holder for this preprint (which was not certified by peer review) is the author/funder, who has granted bioRxiv a license to display the preprint in perpetuity. It is made available under aCC-BY-NC 4.0 International license.

185 augmentation improved rhodopsin degradation in R218C and N296H iPSC-RPE, but not in A146K iPSC-
186 RPE (**Figure 3E and S2J-L**).
187
188 **Gene editing specifically targets the mutant allele in A146K adBD iPSC-RPE and restores CaCC**
189 **activity.**
190 To determine whether A146K iPSC-RPE would respond to an alternative therapeutic approach,
191 we tested gene editing as a means to eliminate expression of the mutant *BEST1* allele. Gene editing with
192 CRISPR-Cas9 creates targeted double strand breaks in genomic DNA that are primarily repaired by
193 endogenous non-homologous end joining (NHEJ) (26), leading to indels. These indels can cause
194 transcriptional frameshifts that lead to premature termination codons, activation of intrinsic nonsense-
195 mediated decay (NMD) pathways, and degradation of transcription products (27, 28).
196 An sgRNA sequence targeting specifically the A146K locus in the mutant *BEST1* allele was
197 cloned into a lentiviral plasmid that encoded both the sgRNA (expressed via a U6 promoter) and a human
198 codon optimized *Streptococcus pyogenes Cas9* (*spCas9)-T2A-GFP* transcript (expressed via a *hVMD2*
199 promoter) (**Figures 4A and 4B**). We also cloned a sgRNA sequence targeting the *AAVS1* safe harbor
200 locus (29) into the same lentiviral plasmid backbone to serve as an experimental control.
201 Two weeks after transduction of A146K adBD iPSC-RPE with A146K sgRNA or control (*AAVS1*
202 sgRNA) lentiviral genome editor, we quantified the average frequency of deep sequencing reads
203 corresponding to WT, mutant, and edited alleles in genomic DNA. We detected a nearly 80% editing
204 frequency of the A146K mutant allele with no decrease in WT allele frequency post-editing (**Figure 4C**).
205 Together, these results reflect efficient editing with high specificity for the A146K mutant allele over the
206 WT *BEST1* allele.

bioRxiv preprint doi: https://doi.org/10.1101/796581; this version posted January 30, 2020. The copyright holder for this preprint (which was not certified by peer review) is the author/funder, who has granted bioRxiv a license to display the preprint in perpetuity. It is made available under aCC-BY-NC 4.0 International license.

207 Using deep sequencing, we next examined specific indels that were introduced into A146K iPSC-
208 RPE two weeks post-transduction with the A146K sgRNA genome editor (**SI data file A**). An average of
209 95.4% of the edited alleles resulted in a frameshift mutation (**Figure 4D and SI data file A**), which is
210 higher than the percentage of out-of-frame indels predicted by a recent machine learning algorithm (**SI**
211 **data file A**) (30). This finding indicates a high likelihood that indels resulting from gene editing at the
212 A146K locus in the mutant *BEST1* allele will trigger NMD of the transcribed RNA, effectively knocking
213 out expression of the mutant allele in the vast majority of edited RPE cells.
214 We next assessed functional rescue of BEST1 channel activity in AAVS1 control versus A146K
215 mutant allele gene-edited iPSC-RPE. Single-cell patch-clamp experiments revealed restoration of CaCC
216 activity in gene-edited A146K iPSC-RPE, but not in control *AAVS1* sgRNA treated A146K iPSC-RPE
217 (**Figure 4E, F and S3**).
218
219 **Mutant allele-specific gene editing restores CaCC activity in all tested adBD iPSC-RPE.**
220 While the gene editing results obtained in the A146K adBD iPSC-RPE model were highly
221 encouraging, it is possible that this locus is unique in its potential to be targeted by a mutant allele-
222 specific sgRNA. To extend this investigation, we also evaluated the specificity and efficacy of gene
223 mutant allele editing in the N296H and R218C adBD iPSC-RPE models. N296H and R218C mutant
224 allele-targeted sgRNAs were designed and cloned into separate lentiviral plasmids as described for the
225 A146K sgRNA. N296H iPSC-RPE and R218C iPSC-RPE were transduced with lentiviral genome editors
226 encoding either control (*AAVS1*) or corresponding allele-targeted sgRNA and editing outcomes were
227 measured via deep sequencing of genomic DNA (**SI data file A**). Quantification of WT and mutant allele
228 frequency revealed efficient targeting of the N296H and R218C mutant alleles with their respective
229 sgRNAs (55.5% and 66.4%, respectively) with no demonstrable targeting of the WT alleles (**Figure 4G,**

bioRxiv preprint doi: https://doi.org/10.1101/796581; this version posted January 30, 2020. The copyright holder for this preprint (which was not certified by peer review) is the author/funder, who has granted bioRxiv a license to display the preprint in perpetuity. It is made available under aCC-BY-NC 4.0 International license.

230 **I**). A high proportion of editing in these two models resulted in out-of-frame indels (96.0% and 94.5% for
231 N296H and R218C iPSC-RPE, respectively) (**Figure 4H, J**). Subsequent single-cell patch-clamp
232 measurements of CaCC current density confirmed restoration of channel activity post-gene editing in both
233 R218C and N296H iPSC-RPE (**Figure 4K-M and S3).** Thus, while some variation in gene editing
234 efficiency was observed using the three different sgRNAs (as expected), more than half of the mutant
235 alleles were edited (with a high percentage of out-of-frame indels) in the three adBD iPSC-RPE models,
236 with no editing of the WT allele.
237
238 **Mutant allele-specific gene editing does not perturb global iPSC-RPE transcriptional programs,**
239 **although off-target editing can occur.**
240 Although the mutant allele-specific sgRNAs tested in the three adBD iPSC-RPE models did not
241 target the fellow WT alleles in any of our experiments, the potential for off-target adverse effects
242 elsewhere within the genome still exists. To detect untoward transcriptional effects from gene editing, we
243 performed single-cell RNA sequencing (scRNA-seq) for 12,061 individual iPSC-RPE cells treated with
244 genome editors. iPSC-RPE (R218C, N296H, A146K, or isogenic control R218C>WT) were edited with
245 genome editors encoding either a mutant allele-targeted sgRNA or a control sgRNA targeting the *AAVS1*
246 site, to generate a total of eight separate samples (**Figure S4A**).
247 Evaluation of t-Distributed Stochastic Neighbor Embedding (t-SNE) clustering of cells across all
248 eight samples indicated that, by virtue of using the *hVMD2* promoter, *spCas9-T2A-GFP* transcript levels
249 closely corresponded with *BEST1* transcript levels (**Figure 5A**). Visual comparison of t-SNE clustering of
250 each individual sample demonstrated that transcriptional signatures are grossly similar between iPSC-
251 RPE lines, whether treated with mutant allele-targeted (+GE) or control (*AAVS1*) sgRNA (**Figure 5B**
252 ***top***). This observation was supported quantitatively by non-negative matrix factorization (NMF). NMF

bioRxiv preprint doi: https://doi.org/10.1101/796581; this version posted January 30, 2020. The copyright holder for this preprint (which was not certified by peer review) is the author/funder, who has granted bioRxiv a license to display the preprint in perpetuity. It is made available under aCC-BY-NC 4.0 International license.

253 analysis demonstrated that greater transcriptome variation exists between iPSC-RPE from different lines
254 than between iPSC-RPE from the same line treated with mutant allele-targeted or control sgRNA (**Figure**
255 **S4B**).

256 Additional analysis of global gene expression (**Figure 5B *bottom***) and of a focused set of genes
257 related to negative or off-target effects (including cell cycle regulation, apoptosis, DNA damage response,
258 or innate immune response; **Figure S4C, SI data file B**) did not reveal significant upregulation of those
259 gene sets in mutant allele-targeted (+GE) versus control sgRNA-treated samples. However, examination
260 of the top nine potential off-target sites for the R218C sgRNA revealed a low, yet significant percentage
261 of editing at a single site within a non-coding region of chromosome 7 (**Figure 5C**). While this finding is
262 not predicted to have a deleterious effect on RPE cell function, it emphasizes the importance of
263 performing comprehensive on- and off-target genome editing analyses using a patient-specific model
264 system.
265

266 **Discussion**

267 The observation that a subset of adBD mutations may be amenable to gene augmentation greatly
268 expands the Best disease patient population that might benefit from this therapeutic approach. Based on
269 the crystallographic studies by Dickson et al. (16), the two mutations that responded to gene augmentation
270 lie within calcium clasp (N296H) or chloride binding (R218C) sites within the BEST1 channel, whereas
271 the mutation that failed to respond (A146K) localizes to a putative structural region. Among the over 200
272 known *BEST1* mutations, many are predicted to be directly or indirectly involved in ion binding (16, 31).
273 Importantly, a recent study by Ji et al. using baculovirus supports our finding that chloride and calcium
274 binding site mutations in BEST1 can be receptive to gene augmentation (32). However, the fact that not

bioRxiv preprint doi: https://doi.org/10.1101/796581; this version posted January 30, 2020. The copyright holder for this preprint (which was not certified by peer review) is the author/funder, who has granted bioRxiv a license to display the preprint in perpetuity. It is made available under aCC-BY-NC 4.0 International license.

275 all adBD iPSC-RPE models respond to gene augmentation underscores the need to vet patient candidacy
276 for gene augmentation carefully.

277 The mechanism underlying selective responsivity of adBD patients to gene augmentation cannot
278 be due to traditional allelic haploinsufficiency, in which half the normal amount of WT protein and no
279 mutant protein is produced, resulting in fewer (but fully WT) BEST1 channels. Such a situation exists in
280 parents of ARB patients, who have no demonstrable disease phenotype. Rather, adBD mutant monomers
281 must be incorporated alongside WT monomers in all (or nearly all) BEST1 channels (33). We propose
282 that in the case of N296H and R218C, this commingling of WT and mutant monomers causes ion binding
283 site insufficiency and channel impermeability, a condition that is surmountable by WT *BEST1*
284 augmentation. In contrast, we hypothesize that *BEST1* mutations like A146K—which converts a nonpolar
285 amino acid to a polar amino acid in a compact structural region of the protein—has more pervasive
286 functional consequences, resulting in greater resistance to gene augmentation.

287 We did consider the possibility that mutation-specific resistance to gene augmentation was due to
288 variability in transgene expression (*i.e.*, there was insufficient WT transgene expression in the non-
289 responsive A146K adBD iPSC-RPE model). However, we found that BEST1 protein levels were similar
290 in all models following gene augmentation. In fact, a slightly higher fold-increase in BEST1 levels was
291 achieved in A146K adBD iPSC-RPE compared with the two adBD models that were rescued by gene
292 augmentation (N296H and R218C). Thus, it is highly unlikely that the differences in functional response
293 observed between R218C or N296H adBD iPSC-RPE and A146K adBD iPSC-RPE are due to variability
294 in transgene expression. Resistance of the A146K mutation to functional recovery after gene
295 augmentation also cannot be explained by occult artifacts inherent to the iPSC line or its RPE progeny,
296 since gene editing was ultimately successful in restoring CaCC activity in the same differentiated A146K
297 adBD iPSC-RPE population.

bioRxiv preprint doi: https://doi.org/10.1101/796581; this version posted January 30, 2020. The copyright holder for this preprint (which was not certified by peer review) is the author/funder, who has granted bioRxiv a license to display the preprint in perpetuity. It is made available under aCC-BY-NC 4.0 International license.

298 It is also notable that our lentiviral constructs employed the *hVMD2* promoter, which is ideal from
299 a translational standpoint as it specifies expression in RPE and supports native regulation of *BEST1*. Use
300 of alternative promoters poses risks of off-target cell effects and/or undesirably low (ineffectual) or high
301 (toxic) levels of protein expression. For construct delivery, we selected lentivirus based on its excellent *in*
302 *vitro* RPE transduction efficiency (17, 25) and its current use in RPE gene therapy trials
303 (ClinicalTrials.gov Identifiers: NCT01367444, NCT01736592) (24). However, our findings are likely
304 applicable across all *in vivo* transgene delivery platforms that possess comparable safety and transduction
305 efficiency profiles. Indeed, Ji et al. observed improvement in CaCC activity in isolated R218H adBD
306 iPSC-RPE cells following constitutive overexpression of WT BEST1 using an AAV delivery vector (32).
307 There is precedence for using patient-specific iPSCs as preclinical efficacy models for gene
308 therapy clinical trials (34). Our work extends this utility by providing a framework for preclinical testing
309 of mutation-specific responses in a genotypically heterogenous disease using the affected cell type. It
310 remains to be determined whether separate adBD iPSC-RPE models will be required to assess suitability
311 of gene augmentation versus gene editing for every mutation, or if a few models can sufficiently represent
312 larger categories of mutations (*e.g.*, ion binding sites or structural regions) (35).
313 For adBD mutations like A146K that are not amenable to gene augmentation, we showed that
314 targeted gene editing holds great promise as an alternative therapy. Indeed, there is a wide spectrum of
315 *BEST1* mutations that could be treated by CRISPR-Cas9 by designing unique mutation-targeted sgRNAs
316 (examples shown in **SI data file D**). While this approach would be costly and time-consuming if separate
317 testing is required for each mutation-specific sgRNA, rapid advances in gene editing technologies and
318 strategies may overcome such limitations. Other gene therapy strategies also exist for dominant ocular
319 diseases; for example, knockdown of both wildtype and mutant allele transcripts with simultaneous
320 introduction of a modified wildtype gene (36). Whether such an approach would be safe and effective for

bioRxiv preprint doi: https://doi.org/10.1101/796581; this version posted January 30, 2020. The copyright holder for this preprint (which was not certified by peer review) is the author/funder, who has granted bioRxiv a license to display the preprint in perpetuity. It is made available under aCC-BY-NC 4.0 International license.

321 adBD mutations that fail to respond to straightforward gene augmentation is not known, but could be
322 tested using the iPSC-RPE model systems employed here.
323 In our gene editing experiments, we observed higher efficiency out-of-frame editing in iPSC-RPE
324 when compared to a prior study using undifferentiated iPSCs (19). This finding is consistent with recent
325 reports of variable mutation bias across different cell types (30), and points to the importance of
326 evaluating gene editing using the specific cell type(s) targeted by disease. In addition, editing at *BEST1* in
327 iPSC-RPE did not provoke an increase in expression of genes associated with cell cycle regulation,
328 apoptosis, DNA damage response, or innate immune response in comparison to editing at a well
329 characterized safe-harbor locus (29) with a previously described sgRNA (37). Undesirable effects such as
330 these have been reported in other cell types following Cas9-mediated gene editing (11, 38). Despite our
331 reassuring findings, there remains the potential for off-target genomic alterations, as was observed at a
332 single locus in a small percentage of iPSC-RPE cells in the R218C adBD model. While these particular
333 off-target indels are in a non-coding region and are thus predicted to be functionally silent, their presence
334 emphasizes the value of employing human model systems for preclinical genome editing safety studies.
335 Interestingly, no off-target indels were detected in our prior study using the same sgRNA in
336 undifferentiated R218C iPSCs (19), which further indicates the need to perform off-target analyses in
337 iPSC-RPE and not in surrogate cell types.
338 Overall, our results provide a blueprint to guide gene therapy choice in the era of gene
339 augmentation and gene editing (**Figure 6**). With its inherently larger target populations and established
340 track record in patients, it is practical to utilize gene augmentation when possible, reserving gene editing
341 for mutations that require allele repair or knockout or are otherwise untreatable by gene augmentation. It
342 is noteworthy that the two adBD lines that demonstrated restoration of CaCC activity with gene
343 augmentation or gene editing did so with equal efficacy, underscoring the suitability of either approach.

bioRxiv preprint doi: https://doi.org/10.1101/796581; this version posted January 30, 2020. The copyright holder for this preprint (which was not certified by peer review) is the author/funder, who has granted bioRxiv a license to display the preprint in perpetuity. It is made available under aCC-BY-NC 4.0 International license.

344 Other desirable characteristics of Best disease as a clinical candidate for gene therapy include 1) a wide
345 time window for gene therapy intervention, 2) accessibility of RPE using standard surgical techniques, 3)
346 a small (~5.5 mm diameter) treatment area, 4) availability of noninvasive retinal imaging and functional
347 assessment tools, and 5) growing patient safety data from other RPE-based gene therapy trials (2-4). As
348 such, Best disease is well-positioned to become the first genotypically heterogeneous disorder with
349 dominant and recessive inheritance patterns to have a full menu of therapeutics for all affected
350 individuals. Furthermore, implications of this work likely extend beyond the eye and Best disease to other
351 intractable monogenic conditions caused by mutations in multimeric ion channels, including congenital
352 myasthenic syndromes and some forms of epilepsy (39-41).
353

354 **Acknowledgements**

355 The authors thank Alfred Lewin (U. Florida) for the *hVMD2-hBEST1-T2A-GFP* plasmid construct; the
356 Cellular Imaging and Analysis core at the University of Wisconsin-Madison Waisman Center; and
357 Andrew Thliveris for helpful discussions. This work was supported by NIH R01EY024588 (to D.M.G.,
358 B.A.T., and E.M.S.); Foundation Fighting Blindness, Research to Prevent Blindness, Retina Research
359 Foundation Emmett Humble Chair, and McPherson Eye Research Institute Sandra Lemke Trout Chair in
360 Eye Research (to D.M.G.); NSF CBET-1350178 and CBET-1645123, NIH R35GM119644, Brain &
361 Behavior Research Foundation, Burroughs Wellcome Fund, and Retina Research Foundation Kathryn
362 and Latimer Murfee Chair (to K.S.); NIH R01EY024995 and Retina Research Foundation M.D. Mathews
363 Professorship (to B.R.P.); NIH T32HG002760 and F30EY027699, VitreoRetinal Surgery Foundation (to
364 B.S.); DGE-1747503 (to K.M.). This study was supported in part by a core grant to the Waisman Center
365 (NICHHD U54 HD090256). We thank members of the Gamm and Saha labs for comments on the
366 manuscript, plasmid depositors to Addgene, the University of Wisconsin-Madison Biotechnology Center

bioRxiv preprint doi: https://doi.org/10.1101/796581; this version posted January 30, 2020. The copyright holder for this preprint (which was not certified by peer review) is the author/funder, who has granted bioRxiv a license to display the preprint in perpetuity. It is made available under aCC-BY-NC 4.0 International license.

367 for DNA sequencing, and the University of Wisconsin-Madison Skin Disease Research Center for
368 assistance with virus preparation.

369

370 **Author contributions**

371 D.S. and D.M.G. designed the gene augmentation experiments. B.S., D.S., D.M.G. and K.S. designed the
372 gene editing experiments. P.K.S. and B.R.P. performed and analyzed the electrophysiology experiments.
373 D.S. and B.S. performed all other experiments with contributions from R.V., K.L.E., C.B, S.S.S., A.A.,
374 and E.C. K.M., S.S., V.P., A.F.S., and S.R. were primarily responsible for the scRNA-seq analysis.
375 B.A.T. and E.M.S. provided and characterized the ARB iPSC line, D.S., B.S., K.S., and D.M.G. wrote the
376 manuscript and analyzed data with input from all authors. D.M.G., K.S., and B.R.P. supervised research.

377

378 **Competing interests statement**

379 The authors declare no competing interests.

bioRxiv preprint doi: https://doi.org/10.1101/796581; this version posted January 30, 2020. The copyright holder for this preprint (which was not certified by peer review) is the author/funder, who has granted bioRxiv a license to display the preprint in perpetuity. It is made available under aCC-BY-NC 4.0 International license.

380 ## Figures and legends

381 # Figure 1

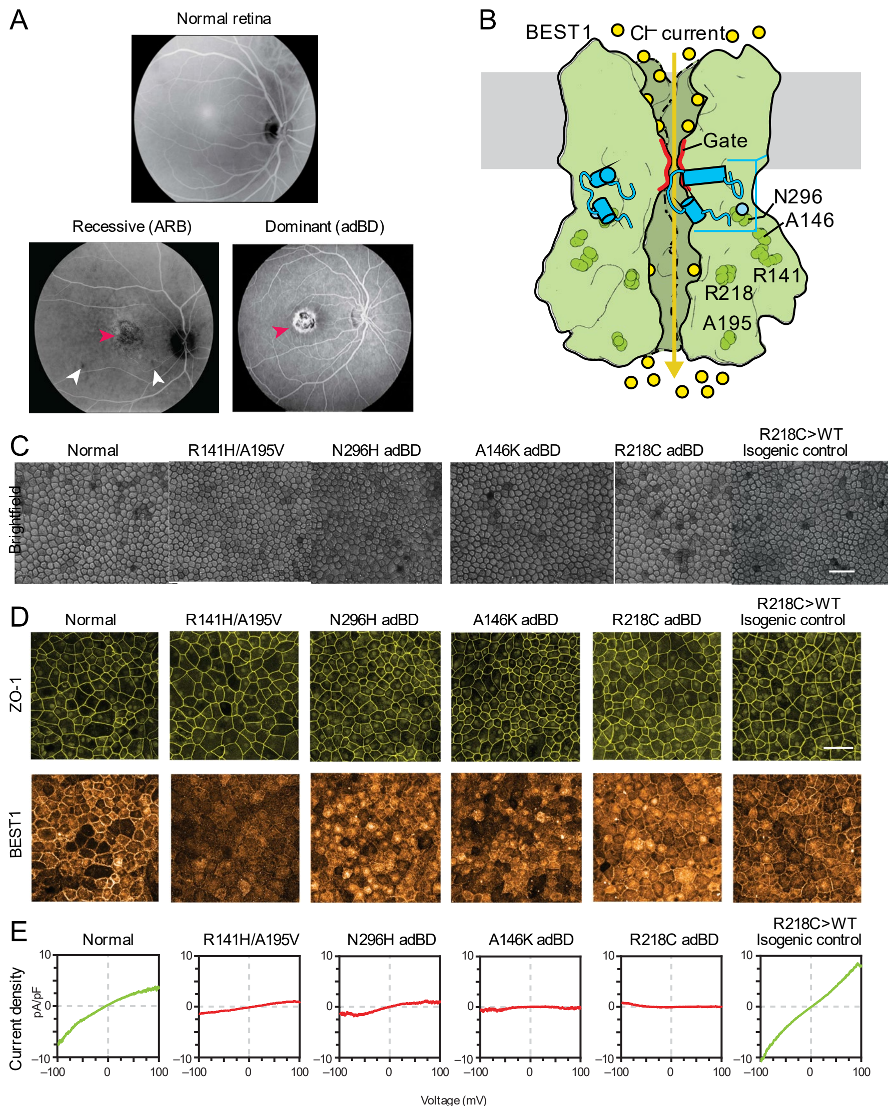

382

383 **Figure 1 | *BEST1* mutations reduce CaCC current in Best disease iPSC-RPE. (A)** *top*, image (in

384 grayscale) of a normal fundus; *bottom left*, fundus image of an ARB patient with R141H/A195V

385 compound heterozygous mutations in *BEST1* showing a vitelliform lesion in the macula (*red* arrowhead)

386 as well as small lesions outside the macula (*white* arrowheads); *bottom right*, fundus image showing a

387 vitelliform macular lesion (*red* arrowhead) in an adBD patient with a heterozygous R218C encoding

388 mutation in *BEST1*. **(B)** A fully functional homo-pentameric BEST1 channel is formed by assembly of

bioRxiv preprint doi: https://doi.org/10.1101/796581; this version posted January 30, 2020. The copyright holder for this preprint (which was not certified by peer review) is the author/funder, who has granted bioRxiv a license to display the preprint in perpetuity. It is made available under aCC-BY-NC 4.0 International license.

389 WT subunits (*green*), allowing movement of chloride ions (*yellow* circles) upon binding of calcium ions
390 (*light blue* circle) (based on the eukaryotic Best1 crystal structure (16)). **(C)** Light microscopic images of
391 normal, patient-specific, and isogenic control iPSC-RPE used in this study. Scale bar = 50 μm (applies to
392 all images in C). **(D)** Immunocytochemical analyses of ZO-1 and BEST1 protein expression in iPSC-RPE
393 cells. Scale bar = 50 μm (applies to all images in D). **(E)** CaCC current density-voltage plots from WT,
394 R141H/A195V ARB, or adBD iPSC-RPE cells, as determined by calculating the difference in average
395 chloride currents in the presence or absence of calcium (Figure S1). For +calcium: n = 6 cells for WT, 12
396 cells for R141H/A195V ARB, 7 cells for N296H adBD, 5 cells for A146K adBD, 5 cells for R218C
397 adBD, and 10 cells for R218C>WT isogenic control; for no calcium: n = 8 cells for WT, 12 cells for
398 R141H/A195V ARB, 8 cells for N296H adBD, 7 cells for A146K adBD, 8 cells for R218C adBD, and 9
399 cells for R218C>WT isogenic control (data combined from at least two replicates).

bioRxiv preprint doi: https://doi.org/10.1101/796581; this version posted January 30, 2020. The copyright holder for this preprint (which was not certified by peer review) is the author/funder, who has granted bioRxiv a license to display the preprint in perpetuity. It is made available under aCC-BY-NC 4.0 International license.

400 **Figure 2**

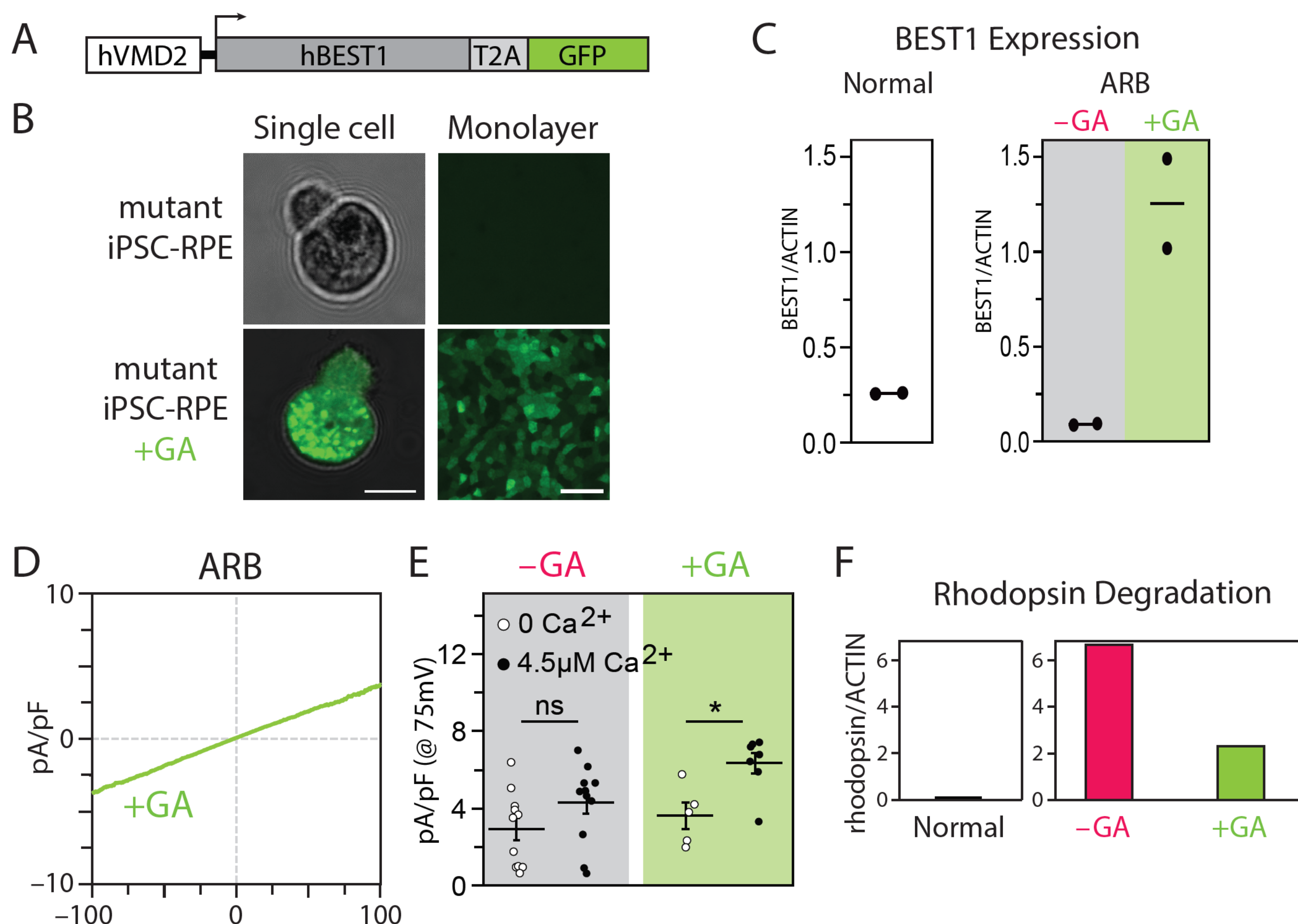

401

402 **Figure 2 | Gene augmentation rescues the ARB iPSC-RPE cell phenotype. (A)** Construct used for

403 *BEST1* gene augmentation (GA). **(B)** Presence or absence of GFP fluorescence in a single dissociated

404 iPSC-RPE cell (*left*) or iPSC-RPE monolayers (*right*) before (*top*) or after (*bottom*) gene augmentation.

405 Scale bar = 10 μm (*left*); 50 μm (*right*). **(C)** Western blot-based quantification of BEST1 protein levels

406 (normalized to ACTIN) in WT iPSC-RPE, ARB iPSC-RPE, and ARB iPSC-RPE after *BEST1*

407 augmentation. **(D)** CaCC current density-voltage plots after gene augmentation in ARB iPSC-RPE. n = 7

408 cells for +calcium and 5 cells for no calcium (data combined from two replicates (Figure S2)). **(E)** CaCC

409 conductance for individual ARB iPSC-RPE cells at 75 mV before or after gene augmentation. The

bioRxiv preprint doi: https://doi.org/10.1101/796581; this version posted January 30, 2020. The copyright holder for this preprint (which was not certified by peer review) is the author/funder, who has granted bioRxiv a license to display the preprint in perpetuity. It is made available under aCC-BY-NC 4.0 International license.

410 number of cells is the same as for panels 1E and 2D. Error bars represent mean ± SEM; ns = p ≥0.05, *
411 for p <0.05. **(F)** Western blot-based quantification of rhodopsin levels 120 hr after photoreceptor outer
412 segment (POS) feeding in WT iPSC-RPE or in ARB iPSC-RPE with or without WT *BEST1* gene
413 augmentation.

bioRxiv preprint doi: https://doi.org/10.1101/796581; this version posted January 30, 2020. The copyright holder for this preprint (which was not certified by peer review) is the author/funder, who has granted bioRxiv a license to display the preprint in perpetuity. It is made available under aCC-BY-NC 4.0 International license.

414 **Figure 3**

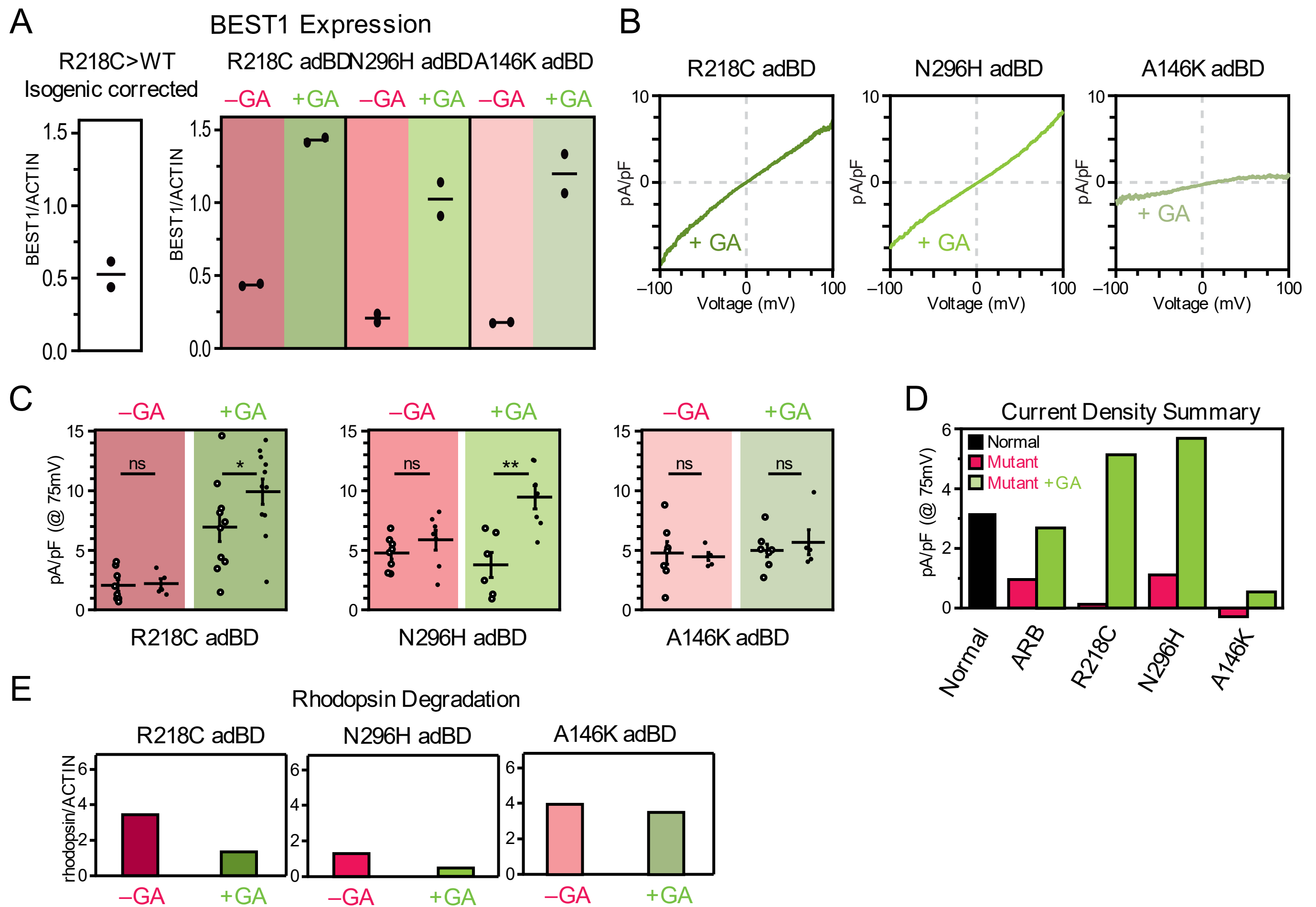

415

416

417 **Figure 3 | Gene augmentation rescues the cell phenotype in some, but not all, adBD iPSC-RPE**

418 **models. (A)** Western blot-based quantification of BEST1 protein levels (normalized to ACTIN) in WT

419 iPSC-RPE and in the adBD iPSC-RPE models before and after *BEST1* gene augmentation (GA). **(B)**

420 CaCC current density-voltage plots after gene augmentation in adBD iPSC-RPE. For +calcium: n = 11

421 cells for R218C, 7 cells for N296H, and 5 cells for A146K; for no calcium: n = 9 cells for R218C, 6 cells

422 for N296H, and 8 cells for A146K (data combined from two replicates). **(C)** CaCC conductance for

423 individual adBD iPSC-RPE cells at 75 mV before and after gene augmentation. The number of cells is the

424 same as for panels 1E and 3B. Error bars represent mean ± SEM; ns = p ≥0.05, * for p <0.05, ** for p

bioRxiv preprint doi: https://doi.org/10.1101/796581; this version posted January 30, 2020. The copyright holder for this preprint (which was not certified by peer review) is the author/funder, who has granted bioRxiv a license to display the preprint in perpetuity. It is made available under aCC-BY-NC 4.0 International license.

<0.01. **(D)** Mean CaCC conductance at 75 mV before or after gene augmentation for all iPSC-RPE tested. **(E)** Rhodopsin levels 48 hours after feeding POS to adBD iPSC-RPE with or without WT *BEST1* gene augmentation.

bioRxiv preprint doi: https://doi.org/10.1101/796581; this version posted January 30, 2020. The copyright holder for this preprint (which was not certified by peer review) is the author/funder, who has granted bioRxiv a license to display the preprint in perpetuity. It is made available under aCC-BY-NC 4.0 International license.

446 **Figure 4**

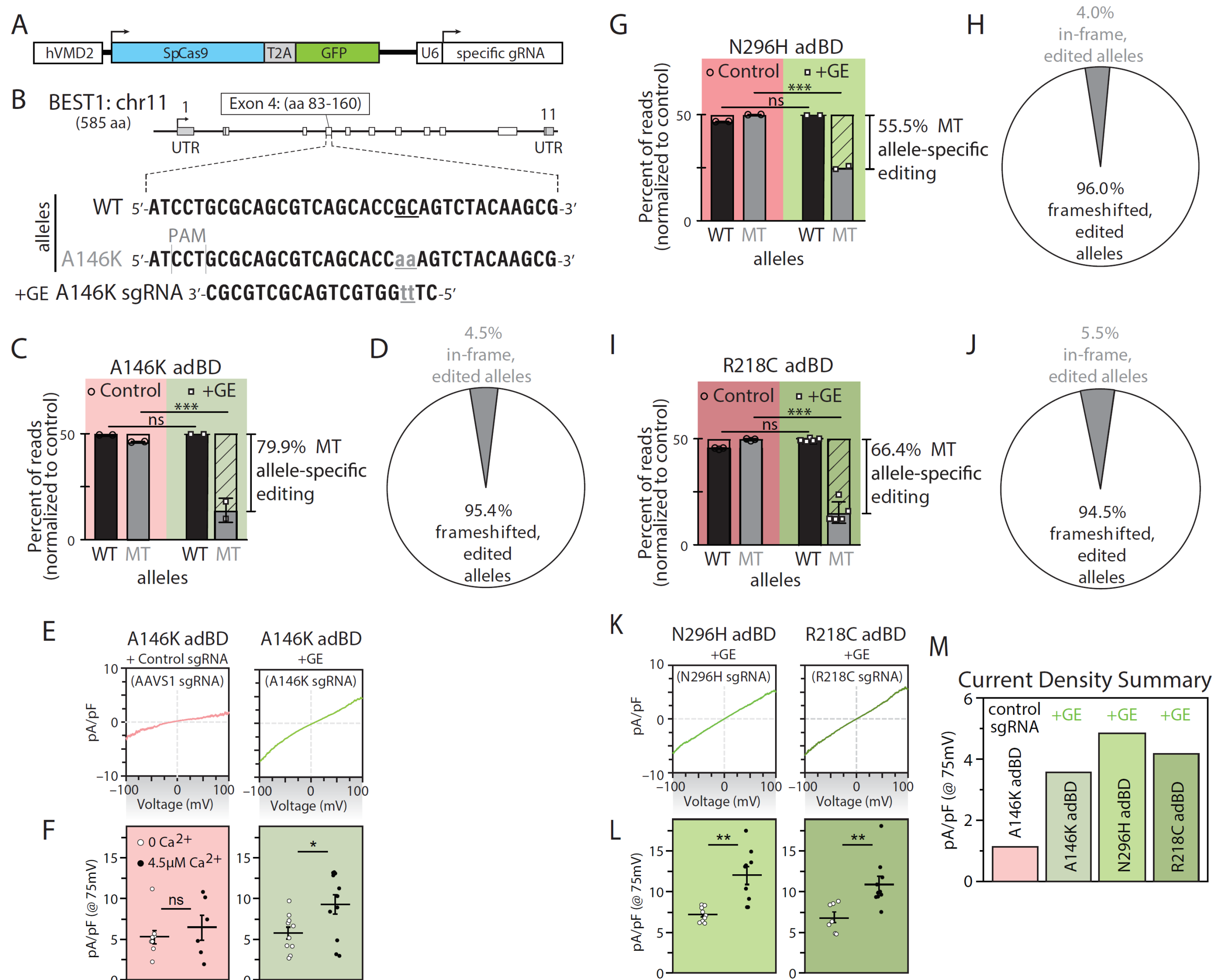

447

448 **Figure 4 | Gene editing specifically and efficiently introduces frameshifts within the mutant allele in**
449 **adBD iPSC-RPE and rescues CaCC activity. (A)** Lentiviral genome editing construct expressing
450 *sp*Cas9 and mutant allele-targeted sgRNAs. **(B)** Diagram showing the heterozygous base pair
451 substitutions in A146K adBD and the design of the A146K sgRNA. The wildtype (WT) allele is shown
452 above, while the A146K adBD allele is shown below, with the mutated bases indicated in lower case and
453 underlined. **(C)** Percentage of WT and mutant (MT; unedited and edited) allele sequencing reads in
454 A146K iPSC-RPE treated with A146K sgRNA lentiviral genome editor ("+GE"), respectively,

bioRxiv preprint doi: https://doi.org/10.1101/796581; this version posted January 30, 2020. The copyright holder for this preprint (which was not certified by peer review) is the author/funder, who has granted bioRxiv a license to display the preprint in perpetuity. It is made available under aCC-BY-NC 4.0 International license.

455 normalized to control ("Control", genome edited with safe harbor *AAVS1*-targeting sgRNA). **(D)** Indel
456 frameshift and in-frame frequency for mutant allele-edited reads from A146K adBD iPSC-RPE
457 (corresponds to 4C). **(E)** CaCC current density-voltage plots and **(F)** CaCC conductance for individual
458 iPSC-RPE cells from single-cell patch clamp experiments for A146K iPSC-RPE treated with control
459 (*AAVS1*) or mutant allele-targeted sgRNA lentiviral genome editor. **(G-J)** Percentage of WT and mutant
460 (MT; unedited and edited) allele sequencing reads in N296H (G) or R218C (I) adBD iPSC-RPE treated
461 with N296H or R218C sgRNA lentiviral genome editor, respectively, normalized to control (*AAVS1*
462 sgRNA). Indel frameshift and in-frame frequency in N296H (H) or R218C (J) adBD iPSC-RPE treated
463 with N296H or R218C sgRNA lentiviral genome editor, respectively (correspond to 4G and 4I,
464 respectively). **(K)** CaCC current density-voltage plots and **(L)** CaCC conductance for individual iPSC-
465 RPE cells from single-cell patch clamp experiments for N296H or R218C adBD iPSC-RPE treated with
466 respective mutant allele-targeted sgRNA lentiviral genome editor. **(M)** Mean CaCC conductance at 75
467 mV for each adBD iPSC-RPE model. The number of cells is the same as 4E and 4K. For gene editing
468 experiments (4C,D and G-J), n = 2 (A146K IPSC-RPE and N296H RPE) and n = 5 (R218C iPSC-RPE).
469 For electrophysiology experiments (4E,F and K-M), +calcium: n = 6 cells for *AAVS1*, 11 cells for A146K,
470 9 cells for N296H, 10 cells for R218C; no calcium: n = 9 cells for *AAVS1*, 10 cells for A146K, 9 cells for
471 N296H, 7 cells for R218C (data combined from two replicates). Error bars in 4C,G,I represent mean ±
472 SD; ns = $p \geq 0.05$, *** for $p < 0.001$. Error bars in 4F and 4L represent mean ± SEM; ns = $p \geq 0.05$, * for p
473 < 0.05, ** for $p < 0.01$.
474
475
476
477

bioRxiv preprint doi: https://doi.org/10.1101/796581; this version posted January 30, 2020. The copyright holder for this preprint (which was not certified by peer review) is the author/funder, who has granted bioRxiv a license to display the preprint in perpetuity. It is made available under aCC-BY-NC 4.0 International license.

478 **Figure 5**

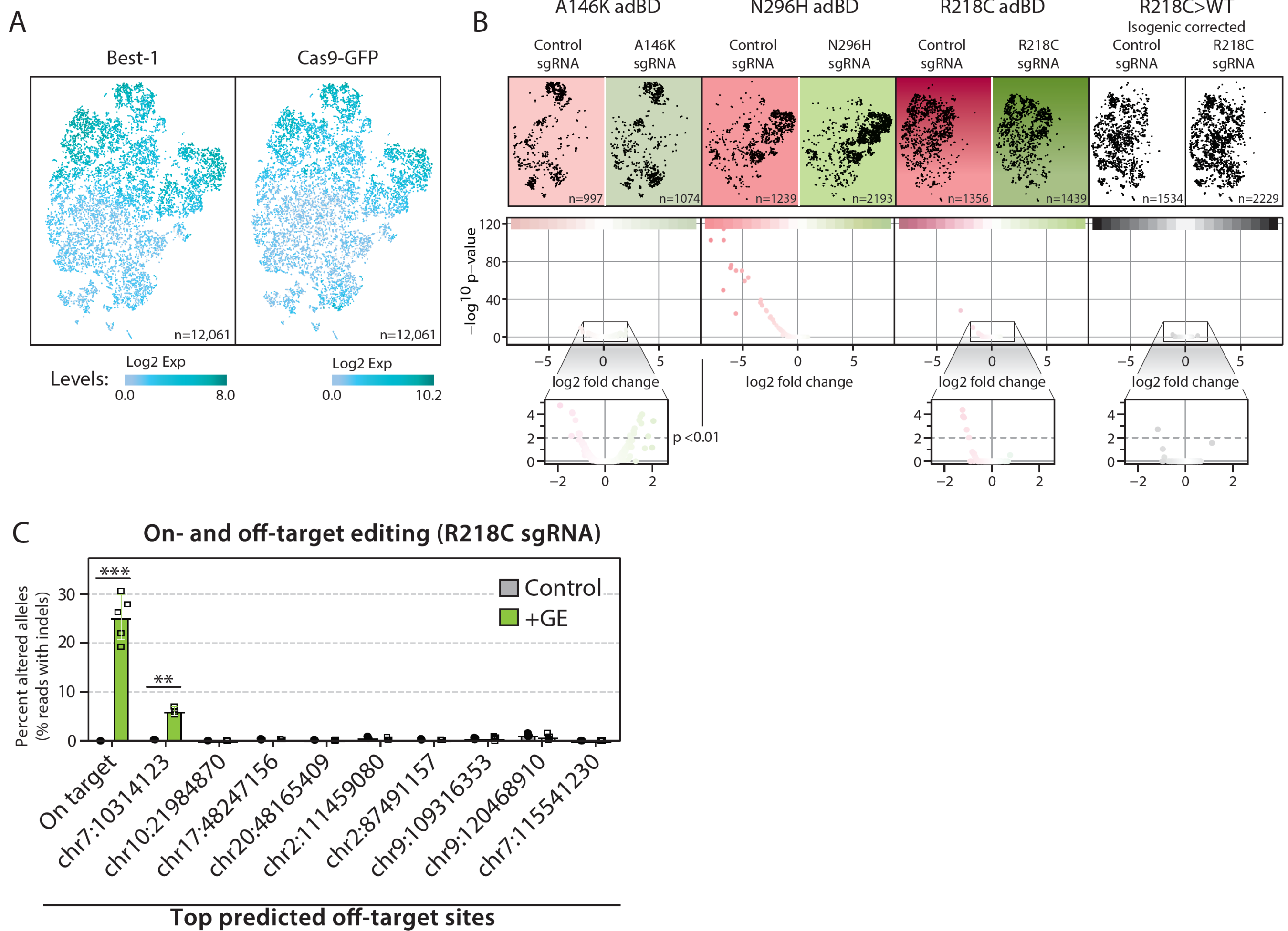

479

480

481 **Figure 5 | Gene editing did not disrupt iPSC-RPE transcriptional programs. (A)** t-SNE plot of single
482 iPSC-RPE cells across all 8 samples with relative expression of *BEST1* (*left*) and *spCas9-T2A-GFP*
483 (*right*) depicted via increasing shades of *blue*. Total number of cells analyzed (n) is shown. **(B)** *Top*, t-
484 SNE plot of single cells (*black* dots) from each treated sample. Number of cells analyzed (n) for each
485 sample is shown. *Bottom*, Volcano plots of transcriptome-wide differences in expression of individual
486 genes (*red* or *green* dots) between iPSC-RPE of the same genotype treated with mutant allele-targeted
487 sgRNA (*green*) versus control (*AAVS1*, *red*) sgRNA lentiviral genome editor. p <0.01 was the threshold

bioRxiv preprint doi: https://doi.org/10.1101/796581; this version posted January 30, 2020. The copyright holder for this preprint (which was not certified by peer review) is the author/funder, who has granted bioRxiv a license to display the preprint in perpetuity. It is made available under aCC-BY-NC 4.0 International license.

488 for determining significant versus non-significant changes in gene expression. **(C)** Frequency of edited
489 alleles at on-target and top nine ranked off-target loci in R218C adBD iPSC-RPE treated with R218C
490 sgRNA lentiviral genome editor (n=3 for control and n=5 for +GE, except n=3 at first *chr 7* off-target
491 locus). Off-target sites are annotated by the location of the first base of the predicted off-target site
492 (further detailed in SI Data File C). Error bars represent mean ± SD; ** for $p < 0.01$, *** for $p < 0.001$.
493
494
495
496
497
498
499
500
501
502
503
504
505
506
507
508

bioRxiv preprint doi: https://doi.org/10.1101/796581; this version posted January 30, 2020. The copyright holder for this preprint (which was not certified by peer review) is the author/funder, who has granted bioRxiv a license to display the preprint in perpetuity. It is made available under aCC-BY-NC 4.0 International license.

509 **Figure 6**

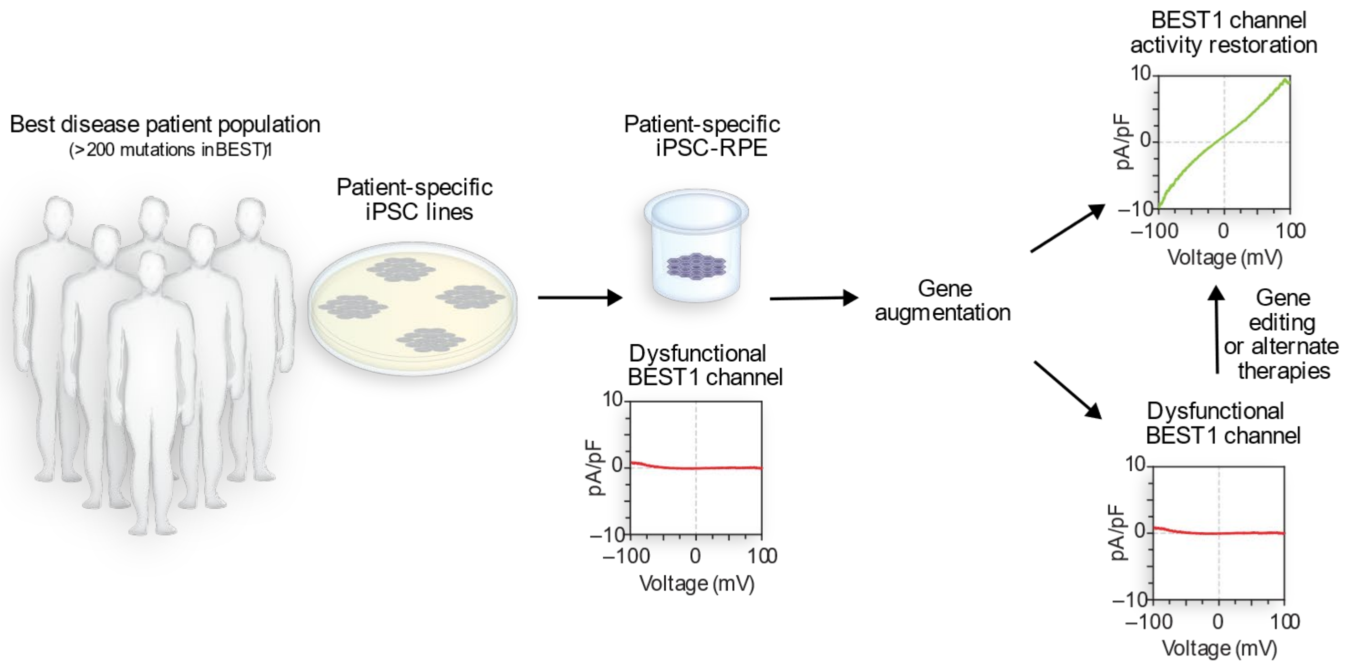

510

511

512 **Figure 6 | In vitro gene therapy testing strategy for adBD.** The amenability of adBD mutations to
513 correction via gene augmentation can be evaluated for efficacy and safety in a dish using patient iPSC-
514 RPE models. Those patients with mutations that fail to respond to gene augmentation would then undergo
515 further testing for genome editing (or another alternative strategy) using the same adBD iPSC-RPE model
516 systems.

bioRxiv preprint doi: https://doi.org/10.1101/796581; this version posted January 30, 2020. The copyright holder for this preprint (which was not certified by peer review) is the author/funder, who has granted bioRxiv a license to display the preprint in perpetuity. It is made available under aCC-BY-NC 4.0 International license.

517 **Materials and Methods**

518 **iPSC lines**

519 A total of 6 iPSC lines, 2 control and 4 patient-specific, were used in this study. In addition to one
520 control iPSC line (normal) and two adBD patient-specific iPSC lines (A146K adBD and N296H adBD)
521 previously used by our group for Best disease modeling (17), we used three new iPSC lines. Two of the
522 new iPSC lines harbored patient specific mutations: R218C for adBD and R141H/A195V for ARB. One
523 isogenic control iPSC line was obtained by CRISPR/Cas9-based gene correction of the patient-specific
524 R218C adBD iPSC line (19). All iPSC lines were cultured either on mouse embryonic fibroblasts (MEFs)
525 or on Matrigel. Lines cultured on MEFs were maintained using iPS media (Dulbecco's Modified Eagle's
526 Medium (DMEM)/F12 (1:1), 20% Knockout Serum Replacement (KOSR), 1% MEM non-essential
527 amino acids, 1% L-glutamine, 0.2 mM β-mercaptoethanol, 100 ng/ml FGF-2), and iPSCs cultured on
528 Matrigel were cultured with either mTeSR1 or StemFlex media. MEFs, FGF-2, and Matrigel were
529 purchased from WiCell (Madison, WI). All other cell culture reagents were purchased from ThermoFisher
530 Scientific. Karyotype analysis was performed as a quality control. The manuscript does not contain
531 human subject or animal studies, and all work with iPSC lines was carried out in accordance with
532 institutional, national, and international guidelines and approved by the Stem Cell Research Oversight
533 Committee at the University of Wisconsin-Madison.

534

535 **Differentiation of iPSC lines to RPE**

536 Differentiation of iPSCs to RPE was performed as previously described (17, 42). Briefly, iPSCs
537 were enzymatically lifted (1 mg/ml dispase for cells cultured on MEFs; 2 mg/ml dispase or 1 ml ReLeSR
538 for cells cultured on Matrigel) to form aggregates, also referred to as embryoid bodies (EBs). EBs were
539 maintained in suspension culture either in EB media (iPS media without FGF-2) and then switched to

bioRxiv preprint doi: https://doi.org/10.1101/796581; this version posted January 30, 2020. The copyright holder for this preprint (which was not certified by peer review) is the author/funder, who has granted bioRxiv a license to display the preprint in perpetuity. It is made available under aCC-BY-NC 4.0 International license.

540 neural induction media (NIM) on day 4, or gradually weaned off mTeSR1/StemFlex and transitioned to
541 NIM by day 4. NIM is composed of 500 ml DMEM/F12 (1:1), 1% N2 supplement, 1% MEM non-
542 essential amino acids, 1% L-glutamine, 2 μg/ml heparin. EBs were plated on laminin (Cat# 23017015)
543 coated 6-well plates (Nunc; Thermo Fisher Scientific) on day 7. On day 16, neural rosettes were
544 mechanically lifted, leaving adherent cells behind that were maintained in retinal differentiation media
545 (RDM; DMEM:F12 (3:1), 2% B27 without retinoic acid, 1% antibiotic-antimycotic solution). For the first
546 four media changes, RDM was supplemented with 10 μM SU5402 and 3 μM CHIR99021.
547 After 60 days of differentiation, pigmented patches of RPE were micro-dissected, dissociated
548 using Trypsin-EDTA (0.25%), and plated on laminin coated surfaces in RDM with 10% FBS and Rho
549 kinase inhibitor (ROCKi; Y-27632). After 2 days, the media was changed to RDM with 2% FBS, and
550 eventually to RDM once the cells were fully confluent. There were no differences observed between RPE
551 differentiated from iPSCs cultured on MEFs and Matrigel. Mutant and wildtype genotypes of iPSC-RPE
552 were verified by Sanger sequencing periodically. Heparin (Cat# H-3149) and SU5402 (Cat# SML0443-
553 25MG) were from Sigma-Aldrich, CHIR99021 (Cat# 4423) was from Tocris Bioscience, and ReLeSR
554 was purchased from STEMCELL Technologies. All other differentiation reagents were purchased from
555 ThermoFisher Scientific.
556
557 **Gene expression analysis**
558 Reverse transcriptase-PCR was used to assess RPE-specific gene expression in RPE derived from
559 different iPSC lines, as described previously (17). Primers used are listed in Table S1.
560
561 **Generation of lentiviral vectors**

bioRxiv preprint doi: https://doi.org/10.1101/796581; this version posted January 30, 2020. The copyright holder for this preprint (which was not certified by peer review) is the author/funder, who has granted bioRxiv a license to display the preprint in perpetuity. It is made available under aCC-BY-NC 4.0 International license.

562 Lentiviral plasmid with the human *VMD2* promoter driving expression of *hBEST1-T2A-GFP* was
563 provided by Alfred S. Lewin (University of Florida). LentiCRISPR v2 (LCv2) plasmid was purchased
564 from Addgene (Cat# 52961). Lentiviral gene editing plasmids containing specific sgRNA sequences and
565 the human *VMD2* promoter driving expression of *spCas9-T2A-GFP* were then generated as described
566 hereafter (all primers and sgRNA sequences are listed in SI Tables). To begin, the '*T2A-GFP-WPRE*'
567 sequence was amplified from the *hVMD2-hBEST1-T2A-GFP* plasmid using LCv2-GFP.Gib.F and .R
568 primers and Q5 2X MM (NEB, Cat# M0492L). The '*2A-Puro-WPRE*' sequence was then removed from
569 the LCv2 plasmid via restriction digestion with PmeI (NEB, Cat# R0560S) and BamHI (NEB, Cat#
570 R3136S). The digestion product was resolved on a 0.7% agarose gel and the plasmid backbone was
571 purified using the Monarch gel purification kit (NEB, Cat# T1020S). The '*T2A-GFP-WPRE*' sequence
572 was inserted into the digested backbone using the Gibson Assembly kit (SGI, Cat# GA1100) per the
573 manufacturer's instructions. The completed Gibson Assembly reaction was then amplified using
574 chemically competent *E. coli* (NEB, Cat# C3040H) and Sanger sequenced to confirm insertion of '*T2A-*
575 *GFP-WPRE*' using LCv2-GFP.seq.L and LCv2-GFP.seq.R primers. This intermediate plasmid product
576 (*pLCv2-GFP*) was digested with AfeI (NEB, Cat# R0652S) and EcoRI-HF (NEB, Cat R310S) to remove
577 the constitutive EF-1 alpha core promoter. The desired digestion product was purified as described above.
578 The *hVMD2* promoter was then PCR amplified from *hVMD2-hBEST1-T2A-GFP* using Q5 2X MM and
579 VMD2.LCv2.GFP.Gib.F and .R primers, followed by insertion into the digested LCv2-GFP backbone via
580 Gibson Assembly. Next, the completed Gibson reaction was transformed into chemically competent *E.*
581 *coli* and the sequence of the final product *hVMD2-spCas9-T2A-GFP* was confirmed via Sanger
582 sequencing using VMD2.LCv2.GFP.seq.L and .R primers. Subsequently, specific sgRNAs were cloned
583 into *hVMD2-spCas9-T2A-GFP* using the restriction digest and Gibson Assembly protocol.
584

bioRxiv preprint doi: https://doi.org/10.1101/796581; this version posted January 30, 2020. The copyright holder for this preprint (which was not certified by peer review) is the author/funder, who has granted bioRxiv a license to display the preprint in perpetuity. It is made available under aCC-BY-NC 4.0 International license.

585 **Lentivirus production and cell transduction**

586 Lentivirus stocks were generated by the Cell Culture Core of the UW Department of Dermatology
587 Skin Disease Research Center (Madison, WI). Briefly, HEK293 cells cultured on 10-cm dishes were
588 transfected with lentiviral plasmids—10 µg of sgRNA encoding lentiviral plasmid (*hVMD2-hBEST1-*
589 *T2A-GFP or hVMD2-spCas9-T2A-GFP*); 5 µg of psPax2 (Addgene, Cat# 12260), and 2 µg of pMD2.G
590 (Addgene, Cat# 12259)—using Lipofectamine (ThermoFisher; Cat# 11668019). After 15 hours, culture
591 medium (DMEM with 10% FBS) was replaced with fresh media containing 1% Penicillin-Streptomycin.
592 Media containing lentiviruses was collected the next day and viral titers were calculated using QuickTiter
593 Lentivirus Titer Kit (Cell Biolabs, Cat# VPK-107). Titers for lentiviral stock were:

Lentivirus	Titer (Transduction units/ml)
hVMD2-hBEST1-T2A-GFP	22x10^{6-7}
hVMD2-spCas9-T2A-GFP R218C sgRNA	74.16 x10^{6-7}
hVMD2-spCas9-T2A-GFP A146K sgRNA	74.26 x10^{6-7}
hVMD2-spCas9-T2A-GFP N296H sgRNA	68.91 x10^{6-7}
hVMD2-spCas9-T2A-GFP AAVS1 sgRNA	74.01 x10^{6-7}

594 For iPSC-RPE transduction, monolayers of iPSC-RPE on transwells were treated with 0, 5, 50, or
595 150 µl (Figure S3) or 150 µl alone of specified lentivirus preparation for all other experiments. Media was
596 changed on day 2 to RDM, and cells were maintained in culture with media changes every 3 days until
597 used for sequencing or other analyses.

598

599 **Transepithelial electrical resistance (TER) measurements**

600 Monolayers of RPE cultured on transwell inserts (Corning, #3470) were used for all TER
601 measurements. To perform the measurements, we employed an epithelial voltohmmeter (EVOM2) with
602 chopstick electrodes (STX2) from World Precision Instruments (Sarasota, USA) according to

bioRxiv preprint doi: https://doi.org/10.1101/796581; this version posted January 30, 2020. The copyright holder for this preprint (which was not certified by peer review) is the author/funder, who has granted bioRxiv a license to display the preprint in perpetuity. It is made available under aCC-BY-NC 4.0 International license.

603 manufacturer's instructions. Electrodes were sterilized with ethanol, and then rinsed in sterile Milli-Q
604 water followed by HBSS before measuring electrical resistance of RPE monolayers. Differences between
605 TER values of transwells with cultured RPE monolayers versus background measurements of cell-free
606 transwell inserts were multiplied by the surface area of the transwell membrane to obtain net TER values
607 in $\Omega \cdot cm^2$.
608

609 **Calcium-activated chloride channel current density measurements**

610 All iPSC-RPE cells used for chloride current measurements were cultured as a monolayer on
611 transwells. To singularize cells prior to measurement, transwells were washed twice with 0 Na-CMF
612 solution (135 mM N-Methyl-D-glucamine (NMDG)-Cl, 5 mM KCl, 10 mM HEPES, 10 mM glucose, 2
613 mM EDTA-KOH, pH adjusted to 7.4) and then incubated with papain enzyme solution (0 Na-CMF
614 solution containing 2.5 µl/ml papain (46 mg/ml, MP Biomedicals LLC, Cat#100921), 0.375 mg/ml
615 adenosine, 0.3mg/ml L-cysteine, 0.25 mg/ml L- glutathione, and 0.05mg/ ml taurine) for 30 minutes at
616 37ºC/5% CO_2. To stop the reaction, 0.01% BSA was added to the enzymatic solution. After washing
617 twice with 0 Na-CMF solution, cells were dispersed in extracellular solution containing 140 mM NaCl, 10
618 mM HEPES, 3 mM KCl, 2 mM $CaCl_2$, 2 mM $MgCl_2$, and 5.5 mM glucose adjusted to pH 7.4 with NaOH
619 by gentle pipetting.

620 Cells with polarized RPE morphology post-dissociation (Figure 2B, *left*) were used to measure
621 chloride currents. To test effects of gene augmentation or gene editing on *BEST1* mutant iPSC-RPE by
622 single-cell patch clamp analysis, only cells with GFP fluorescence (from transduction with *hVMD2-*
623 *hBEST1-T2A-GFP* for gene augmentation or *hVMD2-spCas9-T2A-GFP* encoding *AAVS1* sgRNA or
624 mutant allele-targeted sgRNAs for gene editing) were used. Current recordings on these cells were
625 performed using the conventional whole-cell patch clamp technique with an Axopatch 200A amplifier

bioRxiv preprint doi: https://doi.org/10.1101/796581; this version posted January 30, 2020. The copyright holder for this preprint (which was not certified by peer review) is the author/funder, who has granted bioRxiv a license to display the preprint in perpetuity. It is made available under aCC-BY-NC 4.0 International license.

626 controlled by Clampex software program via the digidata 1550 data acquisition system (Axon
627 Instruments, CA). Fire-polished borosilicate glass pipettes with 3-5 MΩ resistance were filled with pipette
628 solution containing 4.5 μM calcium or no calcium.

629 Recordings were carried out at room temperature and current-voltage tracings were established
630 using ramps from -100 to +100 mV for 1000 ms. The pipette solution with calcium was comprised of (in
631 mM) 146 CsCl, 5 (Ca^{2+})-EGTA-NMDG, 2 $MgCl_2$, 8 HEPES, and 10 sucrose at pH 7.3, adjusted with
632 NMDG. Another pipette solution devoid of calcium was comprised of (in mM) 146 CsCl, 5 EGTA-
633 NMDG, 2 $MgCl_2$, 8 HEPES, and 10 Sucrose at pH 7.3, adjusted with NMDG. Both of these pipette
634 solutions were mixed to make the solution containing 4.5 μM free calcium as described previously(43),
635 which was then used for patch clamping.

636 Current density values were obtained by dividing current amplitude with cell capacitance
637 measurements. CaCC current densities for iPSC-RPE are represented as differences between mean 4.5
638 μM calcium response and mean no calcium response from a total of at least five cells for each condition.
639 At least two differentiations were used as replicates to obtain data for each line.

640

641 **Immunocytochemistry**

642 iPSC-RPE cultured on transwell inserts were washed with PBS and fixed with 4%
643 paraformaldehyde for 10 minutes at room temperature (RT). After washing fixed cells three times with
644 PBS, transwell membranes were placed in blocking solution (10% normal donkey serum with 5% BSA,
645 1% fish gelatin and 0.5% Triton-X100 in PBS) for one hour at RT, and then incubated overnight at 4 ºC
646 in primary antibody (1:100 mouse anti-Bestrophin (Millipore, Cat# MAB5466); 1:100 rabbit anti-ZO-1
647 (ThermoFisher Scientific, Cat# 61-7300)) prepared in blocking solution. Cells were then washed three
648 times in PBS and incubated for 30 minutes at RT in appropriate secondary antibody (ThermoFisher

bioRxiv preprint doi: https://doi.org/10.1101/796581; this version posted January 30, 2020. The copyright holder for this preprint (which was not certified by peer review) is the author/funder, who has granted bioRxiv a license to display the preprint in perpetuity. It is made available under aCC-BY-NC 4.0 International license.

649 Scientific; 1:500 Donkey anti-Mouse IgG (Cat# A31571); 1:500 Donkey anti-Rabbit IgG (Cat# A10040))
650 prepared in blocking solution. Cells were again washed three times in PBS, incubated in DAPI (1:500;
651 ThermoFisher; Cat# D1306) for 30 minutes, mounted using prolong gold with DAPI (ThermoFisher; Cat#
652 P36931), and imaged using Nikon A1R confocal microscope with NIS Elements AR 5.0 software.
653

654 **Rhodopsin degradation assay**

655 Photoreceptor outer segment (POS) feeding of iPSC-RPE was performed as described previously (17).
656 Briefly, bovine POS (InVision BioResources (Seattle, WA)) were gently resuspended in DMEM. 100 µl
657 media was then removed from each transwell insert, 6.25×10^6 POS were added, and cells were incubated
658 at 37 ºC and 5% CO_2 for 2 hours. Afterward, POS containing RDM was removed and each transwell was
659 washed thoroughly three times using DPBS. Following the washes, cells were harvested (0 time point) or
660 further incubated in fresh RDM for prescribed periods of time. At each time point, transwells were
661 washed, 100 µl RIPA buffer (ThermoFisher; Cat# 89900) containing protease inhibitor cocktail (Sigma-
662 Aldrich; Cat# P8340) was added, and cells were incubated on ice for 30 minutes to extract total cell
663 protein. Protein quantification was performed using the DC Protein assay kit II (Bio-Rad, Cat# 5000112).

664 Western blots were then performed to monitor rhodopsin degradation as described (17, 18).
665 Briefly, protein lysates were denatured in 1X Laemmli buffer (reducing) and kept on ice for 10 minutes.
666 Protein samples were then separated on 4-20% mini-Protean TGX gels (Bio-Rad; Cat# 4568095) and
667 electroblotted onto PVDF membranes (Millipore; IPFL10100). After blotting, membranes were dried at
668 RT for 15 minutes, re-activated in methanol for 1 minute, and then incubated in blocking buffer (1:1
669 Odyssey blocking buffer (LI-COR Biosciences; Cat# 927-40000):PBS) for 1 hour. Post-blocking, blots
670 were incubated in primary antibodies (1:500 mouse anti-rhodopsin (Millipore, Cat# MABN15); 0.1 µg/ml
671 rabbit anti-beta actin (Abcam, Cat# ab8227)) in blocking buffer with 0.1% Tween-20 overnight, washed

bioRxiv preprint doi: https://doi.org/10.1101/796581; this version posted January 30, 2020. The copyright holder for this preprint (which was not certified by peer review) is the author/funder, who has granted bioRxiv a license to display the preprint in perpetuity. It is made available under aCC-BY-NC 4.0 International license.

672 three times for 5 minutes each in PBS with 0.1% Tween-20, incubated for 1.5 hours at RT in appropriate
673 secondary antibody (LI-COR Biosciences; 1:20,000 Donkey anti-Rabbit IgG (Cat# 926-32213); 1:20,000
674 Donkey anti-Mouse IgG (Cat# 926-68022)) in blocking buffer with 0.1% Tween-20 and 0.01% SDS, and
675 then washed three times for 5 minutes each in PBS with 0.1% Tween-20. An Odyssey infrared Imager
676 (LI-COR Biosciences) was used to image blots using Image Studio software. ImageJ was used for
677 quantification of relevant protein bands. Samples from rhodopsin degradation assays were also used to
678 assess levels of BEST1 protein before and after gene augmentation. Western blots were performed as
679 described above, using 1:1000 rabbit anti-Bestrophin1 antibody (LAgen Laboratories; Cat# 016-Best1-01)
680 and 1:1000 mouse anti-Actin antibody (Millipore; Cat# MAB1501) as primary antibodies.
681

682 **Deep sequencing analysis of DNA and RNA read frequency**

683 Cells were singularized with TrypLE Express (Gibco, Cat# 12605010) per manufacturer's
684 instructions. Total DNA and/or RNA was extracted using QuickExtract DNA (Epicentre, Cat# QE09050)
685 or QuickExtract RNA (Epicentre, Cat# QER090150), respectively. Both DNA and RNA extractions were
686 performed per manufacturer's instructions with the following minor modifications: 1) a ratio of 10,000-
687 25,000 cells per 50 µl of QuickExtract solution was routinely used, and 2) an optional DNase 1 treatment
688 was omitted from the RNA extraction protocol. All samples were stored at -80 ºC until use.
689 RNA was reverse transcribed to cDNA using the ProtoScript II First Strand synthesis kit (NEB, Cat#
690 E6560S) and synthesis was performed with the "random primer" option included within the kit. 4 µl of
691 crude RNA extract was added to each cDNA reaction.

692 In preparation for targeted deep sequencing, Illumina adapter sequences and sample-specific
693 barcodes were appended to genomic or cDNA amplicons via overhang PCR as described (19). Purified
694 amplicon libraries were assembled into 2 nM total DNA in DNAse/RNAse free H_2O and sequenced using

bioRxiv preprint doi: https://doi.org/10.1101/796581; this version posted January 30, 2020. The copyright holder for this preprint (which was not certified by peer review) is the author/funder, who has granted bioRxiv a license to display the preprint in perpetuity. It is made available under aCC-BY-NC 4.0 International license.

695 150 nucleotide paired end reads using MiSeq (6M or 15M total reads) at the UW Biotech Center
696 (Madison, WI) with the following loading condition: 8 pmol total DNA and 15% PhiX DNA. Raw
697 FASTQ files were read and aligned to expected amplicons using a command line implementation of
698 CRISPResso (v1.0.8) (44). Full commands used for analysis are available upon request. 'Percent allele
699 identity' or 'percent edited' were determined using the software's standard output table of individual read
700 identities. Sequencing reads with counts <100 were not included in the analysis. All FASTQ files are
701 available upon request.
702
703 **Single-cell RNA sequencing (scRNA-seq)**
704 iPSC-RPE cultures derived from the A146K, N296H, and R218C adBD patient lines, and from an
705 isogenic gene-corrected control line derived from the R218C line (R218C>WT) were transduced with 150
706 µl of *hVMD2-spCas9-T2A-GFP* encoding specific sgRNAs as described in the 'Lentivirus production
707 and cell transduction' section. For each sample, sgRNAs were either targeted to mutant *BEST1* or to the
708 *AAVS1* locus (control). On day 14, cells were dissociated from transwells with a papain dissociation kit
709 (Worthington Biochemical, Cat# LK003150) and filtered using a Flowmi cell strainer (Bel-Art SP
710 Scienceware, Cat# H13680-0040) to obtain single-cell suspension. Cells were then prepared for scRNA-
711 seq with the droplet-based 10X Genomics GemCode platform according to the manufacturer's
712 instructions. In brief, singularized cells were encapsulated in oil beads containing a unique molecular
713 identifier (UMI) barcode. The cells were then lysed and cDNA libraries were created featuring cell and
714 transcript-specific molecular identifiers. Libraries were sequenced using an Illumina HiSeq2500 Rapid
715 Run and reads were aligned to a custom reference genome consisting of the human hg19 GRCh38
716 genome and an added gene for the *spCas9-T2A-GFP* transcript.
717

bioRxiv preprint doi: https://doi.org/10.1101/796581; this version posted January 30, 2020. The copyright holder for this preprint (which was not certified by peer review) is the author/funder, who has granted bioRxiv a license to display the preprint in perpetuity. It is made available under aCC-BY-NC 4.0 International license.

718 **scRNA-seq data analysis**

719 Gene edited iPSC-RPE were clustered based on their genome-wide transcriptome using the t-
720 Distributed Stochastic Neighbor Embedding (t-SNE) algorithm with the 10X Genomics Loupe Cell
721 Browser software (v2.0.0). Reads for each pair of samples (*BEST1* mutant allele-targeted sgRNA vs
722 *AAVS1* sgRNA control) were aligned, analyzed, clustered with Cell Ranger v2.1.1, and compared to
723 detect significant differences in gene expression, with p values adjusted using the Benjamini-Hochberg
724 correction for multiple tests. P <0.01 was used as the significance threshold for all analyses. Cell Ranger
725 using the aggregate feature was run to concatenate each pair of samples with the same genotype, and
726 differential gene expression within each pair (with gene editing at either the *AAVS1* or *BEST1* locus) was then
727 analyzed. Potential adverse events were probed using gene lists curated from gene ontology terms
728 associated with the cell cycle, apoptosis, DNA damage response, and the innate immune response, as well
729 as a list of 149 validated marker genes associated with human RPE (45) (**SI data file B**; gene ontology
730 sets are available on the Molecular Signatures Database
731 <http://software.broadinstitute.org/gsea/msigdb>). Differentially-expressed genes with p <0.01 were
732 deemed to be significant. All significantly differentially-expressed genes per cluster are reported, with the
733 exception of genes identified by Cell Ranger as having low average UMI counts. Volcano plots were generated
734 in RStudio (v.1.1.456) using the ggplot2 package.

735

736 **Non-negative matrix factorization-based comparison of scRNA-seq datasets**

737 Non-negative matrix factorization (NMF) followed by clustering of genes using the NMF factors was
738 used for Figure S4 to project each dataset into a gene group. The input data for this analysis were a set of gene
739 barcode matrices generated using the Cell Ranger 2.1.1 algorithm. The matrices were filtered to remove

bioRxiv preprint doi: https://doi.org/10.1101/796581; this version posted January 30, 2020. The copyright holder for this preprint (which was not certified by peer review) is the author/funder, who has granted bioRxiv a license to display the preprint in perpetuity. It is made available under aCC-BY-NC 4.0 International license.

740 background barcodes in order to include only detected cellular barcodes, and then further filtered to exclude
741 cells expressing fewer than 2000 total counts, followed by depth normalization.
742 To enable comparison of transcriptional signatures from each sample, NMF (46) was applied to
743 each scRNA-seq dataset. NMF is a popular dimensionality reduction and clustering approach that is used
744 to project data into low dimensional non-negative factors, and thus can be used to derive a clustering of
745 cells and genes. NMF with k=10 factors was applied with a total of five NMF runs. Next, the similarity of
746 NMF results was compared between two samples using the average best Jaccard coefficient between
747 clusters of one versus another sample. 1-average Jaccard coefficient was then used as the distance to
748 apply hierarchical clustering on the samples. This procedure was repeated five times and the tree that
749 appeared most often was used. The trees learned in different iterations were largely similar and always
750 grouped the patient-specific lines first before grouping different lines together.
751

752 **Quantification and statistical analysis**

753 Unless otherwise specified, all analyses were performed using GraphPad Prism (v.8.0.1) and error
754 bars represent mean ± SD; ns = p ≥0.05, * for p <0.05, ** for p <0.01, *** for p <0.001, **** for p
755 <0.0001. Further detail for each analysis is provided here. Statistical analyses for Figures 2E, 2I and 4B
756 were performed using Origin 2018b. Student's *t*-test was performed to measure the significance between
757 the groups. P values <0.05 were considered statistically significant. Statistical significance for Figure 4D
758 and S3C was determined using the Holm-Sidak method with alpha = 0.05. Each row was analyzed
759 individually, without assuming a consistent SD (number of *t* tests = 10 and 2 for Figure 4D, and S3C,
760 respectively). Statistical significance for differential gene expression in Figures 4F and Figure S4G was
761 determined using the Cell Ranger 2.1.1 algorithm. Sample pairs with each genotype were analyzed and
762 clustered with individual Cell Ranger runs for each pair and analyzed using the Loupe Cell Browser (v.2.0.0).

bioRxiv preprint doi: https://doi.org/10.1101/796581; this version posted January 30, 2020. The copyright holder for this preprint (which was not certified by peer review) is the author/funder, who has granted bioRxiv a license to display the preprint in perpetuity. It is made available under aCC-BY-NC 4.0 International license.

763 Differential expression was calculated using a negative binomial exact test, and p values were adjusted using
764 the Benjamini-Hochberg correction for multiple tests. P <0.01 was used as the threshold for assigning
765 significant versus non-significant changes in gene expression. Volcano plots were generated in RStudio (v
766 1.1.456) using the ggplot2 package. For Figures 3K, L, M, and S3B, discovery was determined using the two-
767 stage linear step-up procedure of Benjamini, Krieger, and Yekutieli with Q = 1%. Each row was analyzed
768 individually, without assuming a consistent SD (number of *t* tests = 3).
769

770 **Data and Software availability**

771 Upon acceptance, scRNA-seq data will be posted to an accession database. Raw targeted
772 sequencing files for DNA and RNA sequencing data will be deposited to the NCBI Trace and Short-Read
773 Archive. Raw patch clamp data are available upon request. Other experimental data are provided in
774 Supplemental files and all source data are available upon request.
775
776
777
778
779
780
781
782
783
784

bioRxiv preprint doi: https://doi.org/10.1101/796581; this version posted January 30, 2020. The copyright holder for this preprint (which was not certified by peer review) is the author/funder, who has granted bioRxiv a license to display the preprint in perpetuity. It is made available under aCC-BY-NC 4.0 International license.

785 **Supporting Information:**

786 # Figure S1

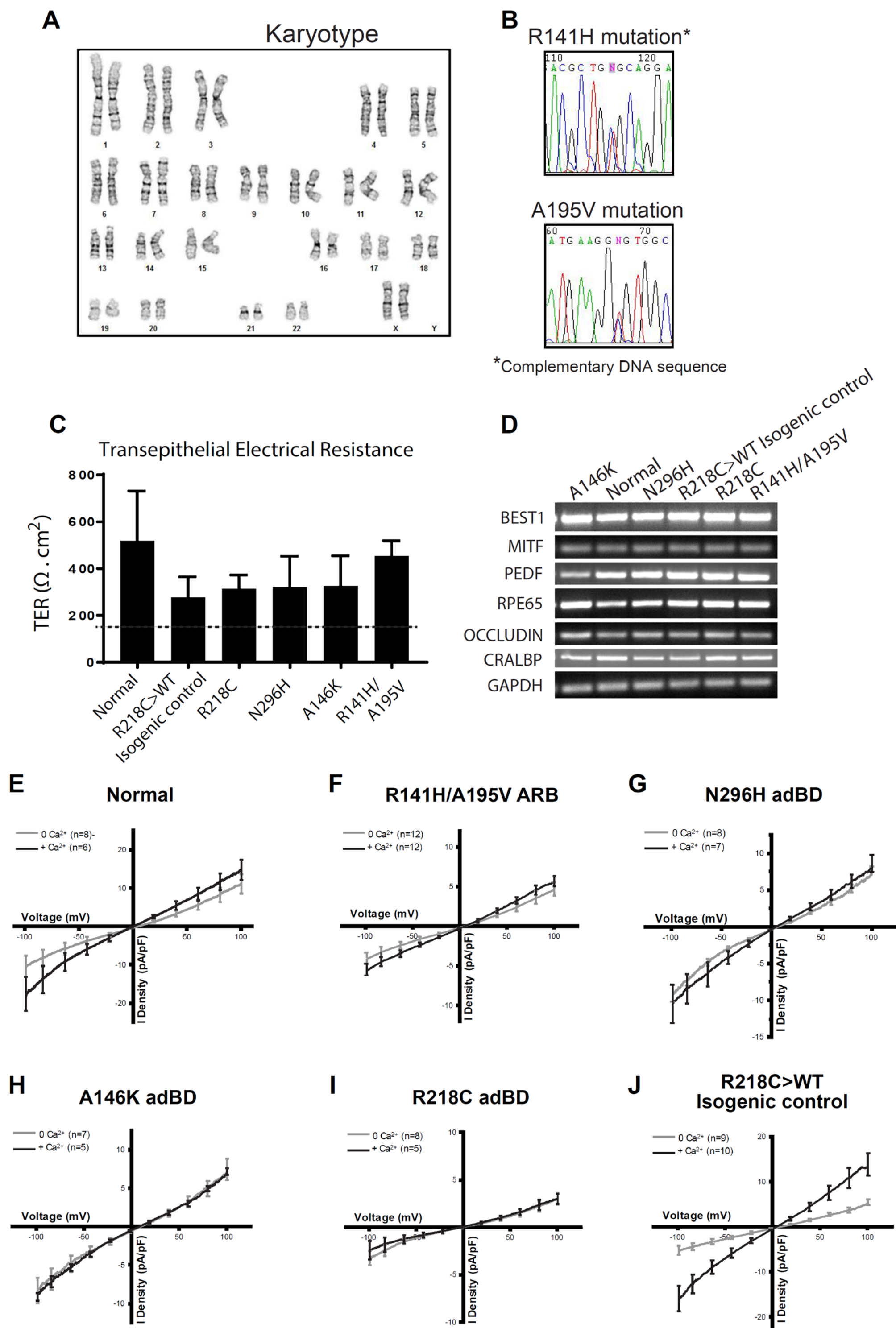

787

bioRxiv preprint doi: https://doi.org/10.1101/796581; this version posted January 30, 2020. The copyright holder for this preprint (which was not certified by peer review) is the author/funder, who has granted bioRxiv a license to display the preprint in perpetuity. It is made available under aCC-BY-NC 4.0 International license.

788 **Figure S1 | Characterization of iPSC-RPE. (A)** Karyotype analysis for ARB iPSCs. **(B)** DNA
789 sequencing confirming R141H and A195V encoding mutations in ARB iPSCs. **(C)** Net transepithelial
790 electrical resistance (TER) ($\Omega \cdot cm^2$) for iPSC-RPE from all six lines. The dashed line demarcates the
791 minimum expected TER (150 $\Omega \cdot cm^2$). Replicates: n=12 for each line (4 transwells from 3 replicates
792 each), error bars represent mean ± SD. **(D)** Gene expression analysis (RT-PCR) of selected RPE-specific
793 markers in all six lines. **(E-J)** Chloride current traces, measured in the presence (*black*) or absence (*gray*)
794 of calcium over a voltage ramp (-100 to +100 mV), that were used to generate CaCC current density plots
795 in Figure 1E. 4.5 μM calcium was used for +calcium conditions. The number (n) of individual cells patch
796 clamped in the presence or absence of calcium in order to calculate CaCC current densities is shown in
797 the top left corner of each graph. Data were obtained from at least two replicates.

bioRxiv preprint doi: https://doi.org/10.1101/796581; this version posted January 30, 2020. The copyright holder for this preprint (which was not certified by peer review) is the author/funder, who has granted bioRxiv a license to display the preprint in perpetuity. It is made available under aCC-BY-NC 4.0 International license.

798 **Figure S2**

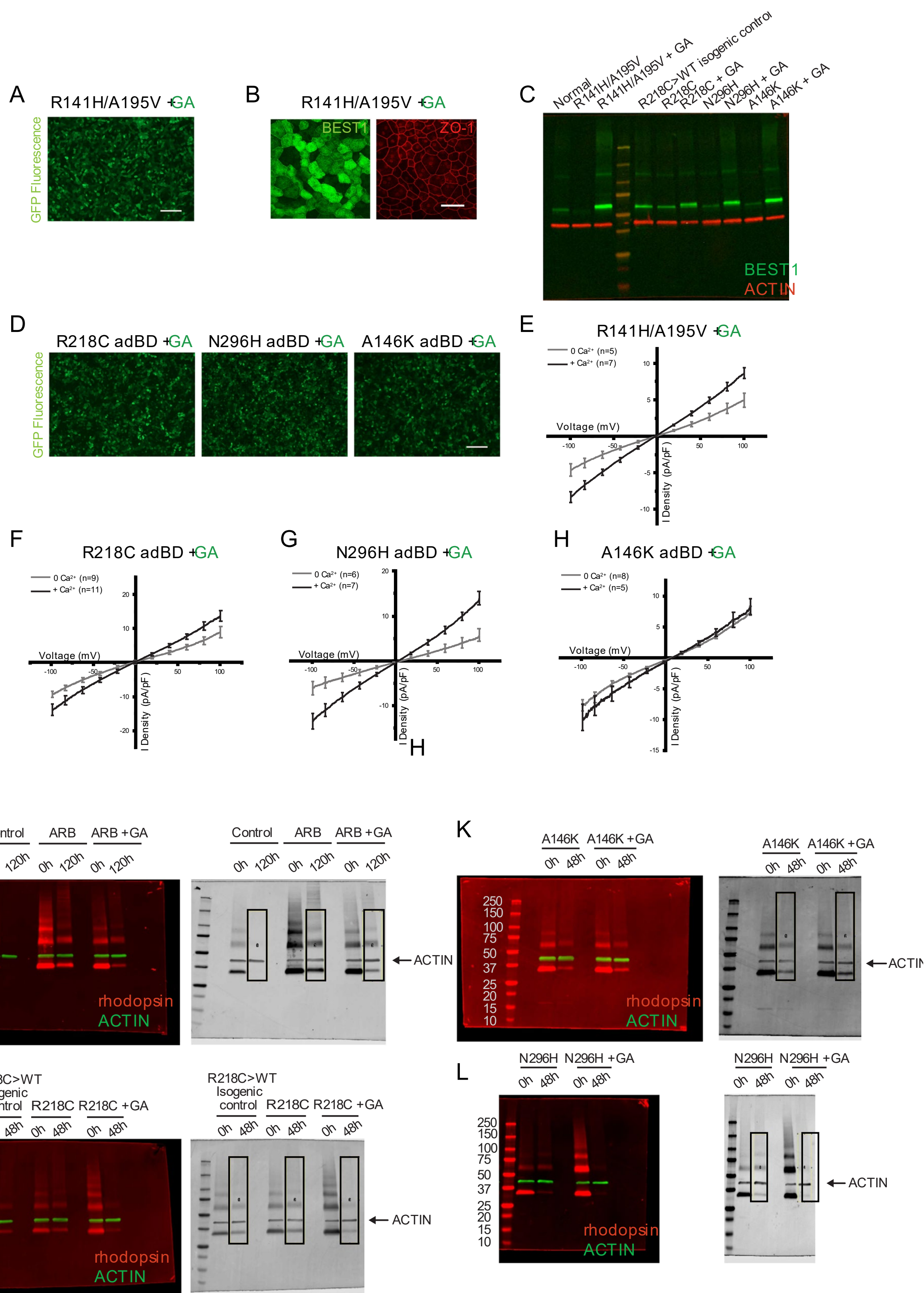

799

bioRxiv preprint doi: https://doi.org/10.1101/796581; this version posted January 30, 2020. The copyright holder for this preprint (which was not certified by peer review) is the author/funder, who has granted bioRxiv a license to display the preprint in perpetuity. It is made available under aCC-BY-NC 4.0 International license.

800 **Figure S2 | Gene augmentation (GA) restores CaCC function in ARB iPSC-RPE and R218C and**
801 **N296H adBD iPSC-RPE, but not in A146K adBD iPSC-RPE. (A)** GFP fluorescence in R141H/A195V
802 ARB iPSC-RPE transduced with lentivirus expressing BEST1. Scale bar = 100 µm. **(B)** ICC analysis of
803 BEST1 and ZO-1 expression in R141H/A195V iPSC-RPE transduced with lentivirus expressing BEST1.
804 Increased BEST1 expression is observed in R141H/A195V iPSC-RPE cells following gene augmentation.
805 Scale bar = 50 µm (applies to both images). **(C)** Representative western blot showing levels of BEST1 in
806 iPSC-RPE. Protein samples from the rhodopsin degradation assays were used to assess BEST1 levels. **(D)**
807 GFP fluorescence in adBD iPSC-RPE transduced with lentivirus expressing hBEST1. Scale bar = 100 µm
808 (applies to all three images). **(E)** Chloride current traces of R141H/A195V iPSC-RPE after gene
809 augmentation measured in the presence (*black*) or absence (*gray*) of calcium. **(F-H)** Chloride current
810 traces for adBD iPSC-RPE after gene augmentation, measured in the presence (*black*) or absence (*gray*)
811 of calcium over a voltage ramp (-100 to +100 mV), that were used to obtain CaCC current density. 4.5
812 µM calcium was used for +calcium conditions. Cells with green fluorescence were used for all patch
813 clamp measurements after gene augmentation. The number (n) of individual cells patch clamped in the
814 presence or absence of calcium (in order to calculate CaCC current densities) is shown in the top left
815 corner of each graph. Data were obtained from at least two replicates. **(I-L)** *left*, Western blots used for
816 the rhodopsin degradation assay, *right*, and corresponding grayscale images of western blots used to
817 quantify levels of rhodopsin shown in Figures 2 and 3 (boxes represent areas used for quantification). For
818 each lane, the boxed area was selected to include bands corresponding to fully denatured rhodopsin and
819 its aggregated forms.
820

bioRxiv preprint doi: https://doi.org/10.1101/796581; this version posted January 30, 2020. The copyright holder for this preprint (which was not certified by peer review) is the author/funder, who has granted bioRxiv a license to display the preprint in perpetuity. It is made available under aCC-BY-NC 4.0 International license.

821 **Figure S3**

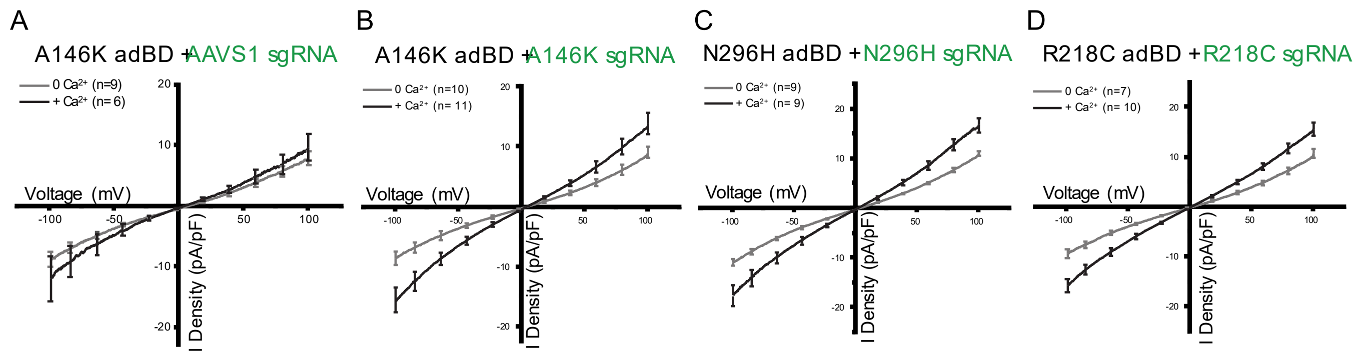

822

823

824 **Figure S3 | Gene editing (GE) restores CaCC activity in iPSC-RPE from all tested adBD lines. (A-**
825 **D)** Chloride current traces, measured in the presence (*black*) or absence (*gray*) of calcium over a voltage
826 ramp (-100 to +100 mV), that were used to calculate CaCC current density plots after gene editing of
827 adBD iPSC-RPE. iPSC-RPE was edited using lentiviral genome editors encoding sgRNA targeting **(A)**
828 *AAVS1* site in A146K adBD iPSC-RPE, **(B)** A146K mutation in A146K adBD iPSC-RPE, **(C)** N296H
829 mutation in N296H adBD iPSC-RPE, or **(D)** R218C mutation in R218C adBD iPSC-RPE. Cells with GFP
830 fluorescence were used for whole cell patch clamp measurements and 4.5 µM calcium was used for
831 +calcium conditions. The number (n) of individual cells patch clamped with or without calcium is shown
832 at the top left corner of each graph. Data were obtained from two replicates.

833

834

835

836

837

838

bioRxiv preprint doi: https://doi.org/10.1101/796581; this version posted January 30, 2020. The copyright holder for this preprint (which was not certified by peer review) is the author/funder, who has granted bioRxiv a license to display the preprint in perpetuity. It is made available under aCC-BY-NC 4.0 International license.

839 **Figure S4**

840 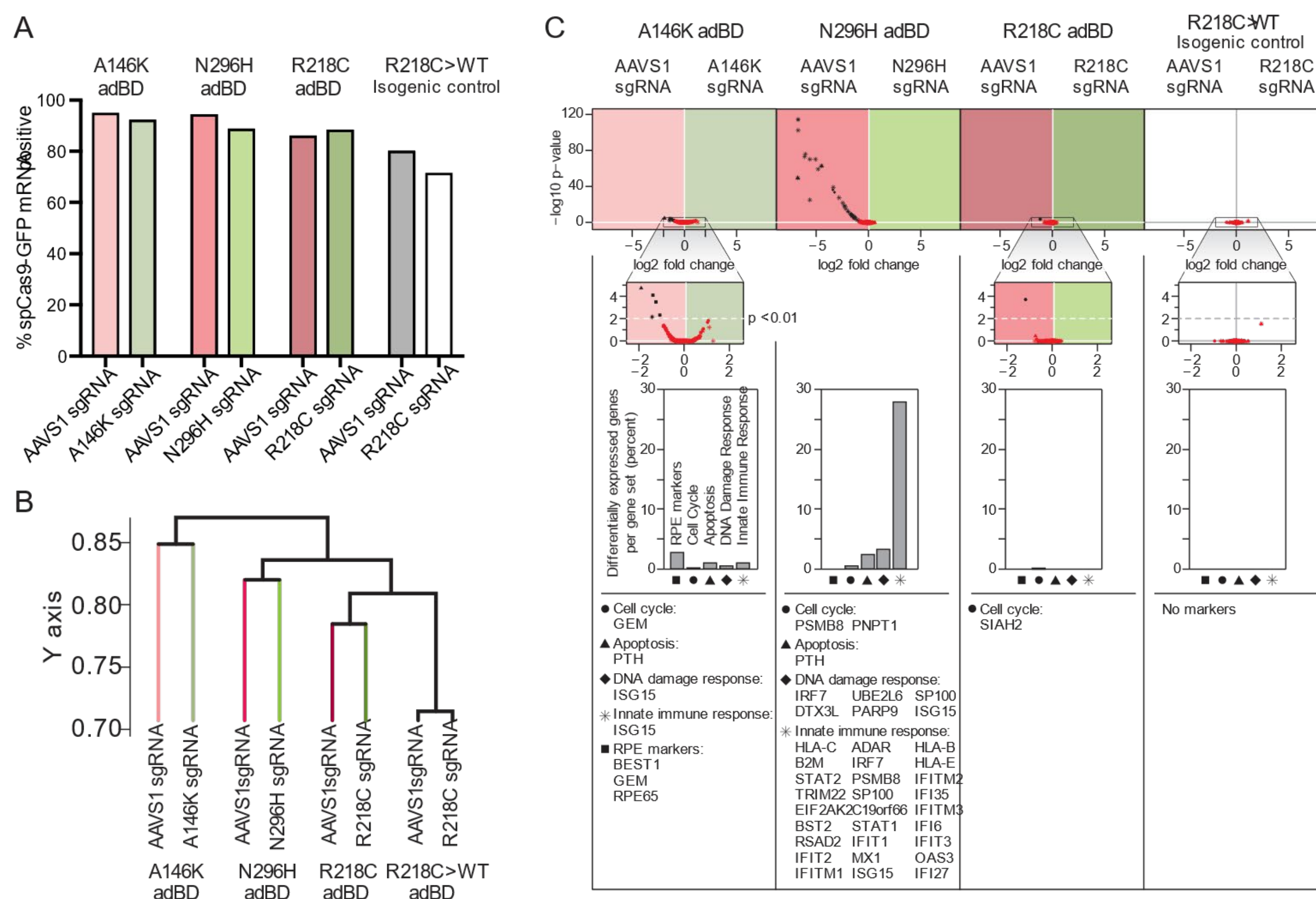

841

842 **Figure S4 | Single cell transcriptome analysis in gene-edited adBD iPSC-RPE. (A)** Percent of
843 analyzed cells per sample for which *spCas9-T2A-GFP* transcripts were captured using scRNA-seq. **(B)**
844 Dendrogram tree depicting relative similarity between samples. Non-negative matrix factorization
845 comparison across samples indicates that greater transcriptional variability exists between iPSC-RPE lines
846 than in the same iPSC-RPE line treated with lentiviral genome editors (*AAVS1* lentiviral genome editor
847 versus *BEST1* mutant allele-targeted lentiviral genome editor). The dendrogram shows the similarity of
848 the transcriptomes from each sample, derived from the average Jaccard coefficient between gene clusters
849 from one sample and those from another sample. The y-axis denotes 1-average Jaccard coefficient and

bioRxiv preprint doi: https://doi.org/10.1101/796581; this version posted January 30, 2020. The copyright holder for this preprint (which was not certified by peer review) is the author/funder, who has granted bioRxiv a license to display the preprint in perpetuity. It is made available under aCC-BY-NC 4.0 International license.

850 indicates the distance between different samples (tree tips) as well as between groups of samples (internal
851 nodes). **(C)** Differential gene expression in 5 curated gene sets associated with cell cycle regulation
852 (*circles*), apoptosis (*triangles*), DNA damage response (*diamonds*), innate immune response (*asterisks*),
853 or RPE-identity (*squares*) in control (*AAVS1*) lentiviral genome editor versus mutant allele-targeted
854 lentiviral genome editor treated samples. For one sample pair (N296H iPSC-RPE), genes associated with
855 a potential adverse treatment effect were upregulated in control lentiviral genome editor-treated sample
856 compared to the mutant allele-targeted lentiviral genome editor sgRNA-treated sample.
857
858 **SI Tables (**attached below**):**
859 Table S1: RPE-specific RT-PCR primers used.
860 Table S2. List of GE vectors used.
861 Table S3. List of primers for lentiviral plasmid generation.
862 Table S4. List of sgRNAs.
863 Table S5. Primers for deep sequencing of DNA and cDNA.
864
865 **SI data files (**available for download**):**
866 SI Data File A. Frameshift analysis of iPSC-RPE+GE.
867 SI Data File B. Curated gene sets used to assess differences in gene expression between control (*AAVS1*)
868 and mutant *BEST1* allele-targeted sgRNA.
869 SI Data File C. Ranked off-target sites for sgRNAs used in this study.
870 SI Data File D. Analysis of additional adBD mutations for amenability to allele-specific editing or
871 scarless base editing.

bioRxiv preprint doi: https://doi.org/10.1101/796581; this version posted January 30, 2020. The copyright holder for this preprint (which was not certified by peer review) is the author/funder, who has granted bioRxiv a license to display the preprint in perpetuity. It is made available under aCC-BY-NC 4.0 International license.

872 **SI Tables:**

873 **Table S1: RPE-specific RT-PCR primers used.**

874

Gene	**Forward Primer**	**Reverse Primer**
BEST1	ATTTATAGGCTGGCCCTCACGGAA	TGTTCTGCCGGAGTCATAAAGCCT
MITF	TTCACGAGCGTCCTGTATGCAGAT	TTGCAAAGCAGGATCCATCAAGCC
PEDF	AATCCATCATTCACCGGGCTCTCT	TGCACCCAGTTGTTGATCTCTTGC
RPE65	GCCCTCCTGCACAAGTTTGACTTT	AGTTGGTCTCTGTGCAAGCGTAGT
OCCLUDIN	TCATTGCCGCGTTGGTGATCTTTG	ATGATGCCCAGGATAGCACTCACT
CRALBP	TTCCGCATGGTACCTGAAGAGGAA	ACTGCAGCCGGAAATTCACATAGC
GAPDH	CAACGGATTTGGTCGTATTGG	GCAACAATATCCACTTTACCACAGTTAA

875
876

bioRxiv preprint doi: https://doi.org/10.1101/796581; this version posted January 30, 2020. The copyright holder for this preprint (which was not certified by peer review) is the author/funder, who has granted bioRxiv a license to display the preprint in perpetuity. It is made available under aCC-BY-NC 4.0 International license.

877 **Table S2. List of gene editing vectors used.**
878

GE Vector Name	sgRNA Name	Vector Backbone	Backbone Source
VMD2.*AAVS1*	*AAVS1*	*hVMD2-spCas9-T2A-GFP*	Alfred Lewin (University of Florida)
VMD2.R218C	R218C	*hVMD2-spCas9-T2A-GFP*	Alfred Lewin (University of Florida)
VMD2.N296H	N296H	*hVMD2-spCas9-T2A-GFP*	Alfred Lewin (University of Florida)
VMD2.A146K	A146K	*hVMD2-spCas9-T2A-GFP*	Alfred Lewin (University of Florida)

879

bioRxiv preprint doi: https://doi.org/10.1101/796581; this version posted January 30, 2020. The copyright holder for this preprint (which was not certified by peer review) is the author/funder, who has granted bioRxiv a license to display the preprint in perpetuity. It is made available under aCC-BY-NC 4.0 International license.

880 **Table S3.** **List of primers for lentiviral plasmid generation.**
881

Primer Name	Primer sequence
LCv2-GFP.Gib.F	GATTACAAAGACGATGACGATAAGGGATCCGGTGAGGGCAGAGGAAGTC
LCv2-GFP.Gib.	ACAGTCGAGGCTGATCAGCGGGTTTAAACCTACTACTGCTAGAGATTTTCCACAC
LCv2-GFP.seq.L	ACCGGCCTGTACGAGACACG
LCv2-GFP.seq.R	GAAAGGACAGTGGGAGTGGCACC
VMD2.LCv2.GFP.Gib.F	GTGGCACCGAGTCGGTGCTTTTTTGAATTCCAATTCTGTCATTTTACTAGGGTGATGAAATTC
VMD2.LCv2.GFP.Gib.R	TGTACTTCTTGTCCATGGTGGCAGCGCTCTATCGGCCGCGGGTACA
VMD2.LCv2.GFP.seq.L	GAATGAATACCGGGCTGCAGTCAAC
VMD2.LCv2.GFP.seq.R	GTCGGTGATCACGGCCCAG

882
883

bioRxiv preprint doi: https://doi.org/10.1101/796581; this version posted January 30, 2020. The copyright holder for this preprint (which was not certified by peer review) is the author/funder, who has granted bioRxiv a license to display the preprint in perpetuity. It is made available under aCC-BY-NC 4.0 International license.

884 **Table S4.** **List of sgRNAs.**
885
886 Off-target (47) and on-target (48) scores are also presented. Scores range from 0-100 with higher scores
887 being better for both scoring systems. Highest ranked off-target cut sites for each sgRNA are available in
888 **SI Data File C**.
889

sgRNA Name	Sequence 5' - 3'	PAM	Chr	Position	Strand	Off-Target Score	On-Target Score
A146K	CTTTGGTGCTGACGCTGCGC	AGG	11	61955893	-1	81.2	51.6
R218C	GTGTCCACACTGAGTACACA	AGG	11	61957403	-1	56.3	67.2
N296H	CATCATCCTCTCCAAAGGGG	TGG	11	61959521	-1	54.0	64.6
AAVS1	GGGGCCACTAGGGACAGGAT	TGG	19	55115755	+1	55.8	54.5

890

bioRxiv preprint doi: https://doi.org/10.1101/796581; this version posted January 30, 2020. The copyright holder for this preprint (which was not certified by peer review) is the author/funder, who has granted bioRxiv a license to display the preprint in perpetuity. It is made available under aCC-BY-NC 4.0 International license.

891 **Table S5.** **Primers for deep sequencing of DNA and cDNA.**
892

Primer Name	Primer sequence
MT.C.OT.5v2.HTS.F	GTTGGTTCCTGAAGATGGGCAG
MT.C.OT.5v2.HTS.R	CTGTCAAGGCCAAGTTCTGCTG
MT.C.OT.2.HTS.F	GCTAAATTCTGCTATAAAAGGAAGG
MT.C.OT.2.HTS.R	GCATTGCTTTAGAAAACTCAGAAGT
MT.C.OT.3.HTS.F	AGTGAGACCAAGTTCTGACAGCA
MT.C.OT.3.HTS.R	GGCCTCTTCATACATACACATGCAC
MT.C.OT.4.HTS.F	CCTCCACATCTGCAGAAAAGTGT
MT.C.OT.4.HTS.R	GGCAGGGTTTGGTCTCCTACTT
MT.C.OT.5.HTS.F	GGATGGCTCTGGGTGGGTTT
MT.C.OT.5.HTS.R	CTTCCAACTCTTCCTCCCACCC
MT.C.OT.6.HTS.F	TGAGGTTCAGAATAGCTCAGCA
MT.C.OT.6.HTS.R	TGTTTCTGTGAAGCAAATCAAAGCT
MT.C.OT.7.HTS.F	TGTTTCTGTGAAGCAAATCAAAGCT
MT.C.OT.7.HTS.R	TGAGGTTCAGAATAGCTCAGCA
MT.C.OT.8.HTS.F	AAAGCATGGCGGGAGTGCTAA
MT.C.OT.8.HTS.R	TGACTAAATCCCTGGCATCGCT
MT.C.OT.9.HTS.F	GCCAGTAATTTTCCAAGGCTTCT
MT.C.OT.9.HTS.R	TTCCTACTAGAACCTCCTTGAG
MT.C.OT.10.HTS.F	GTGACCTGACTTTGCTGAAAGGT
MT.C.OT.10.HTS.R	ACCTGAATTATCTCAAGCTCACT
AAVS1T2.HTS.F	ATGTGGCTCTGGTTCTGGGTAC
AAVS1T2.HTS.R	GAGACTAGGAAGGAGGAGGCCT
R218C.HTSv2.F	GTGTTCAGAACCCCATCCCC
R218C.HTSv2.R	AGCCTAGTCCTCACCTGTGT
BEST.cDNA.HTSv2.F	GGTCGAATCCGGGACCCTATC
BEST.cDNA.HTSv2.R	GCCACAGTCACCACCTGTGTAT
AAVS1T2.HTS.F	ATGTGGCTCTGGTTCTGGGTAC
AAVS1T2.HTS.R	GAGACTAGGAAGGAGGAGGCCT

893
894

bioRxiv preprint doi: https://doi.org/10.1101/796581; this version posted January 30, 2020. The copyright holder for this preprint (which was not certified by peer review) is the author/funder, who has granted bioRxiv a license to display the preprint in perpetuity. It is made available under aCC-BY-NC 4.0 International license.

895 **References**

896 1. J. A. Doudna, E. Charpentier, The new frontier of genome engineering with CRISPR-Cas9. *Science* **346**,
897 1077-+ (2014).
898 2. B. L. Lam *et al.*, Choroideremia Gene Therapy Phase 2 Clinical Trial: 24-Month Results. *Am J Ophthalmol*
899 **197**, 65-73 (2019).
900 3. C. Cukras *et al.*, Retinal AAV8-RS1 Gene Therapy for X-Linked Retinoschisis: Initial Findings from a Phase
901 I/IIa Trial by Intravitreal Delivery. *Mol Ther* **26**, 2282-2294 (2018).
902 4. S. Russell *et al.*, Efficacy and safety of voretigene neparvovec (AAV2-hRPE65v2) in patients with RPE65-
903 mediated inherited retinal dystrophy: a randomised, controlled, open-label, phase 3 trial. *Lancet* **390**, 849-
904 860 (2017).
905 5. H. Ledford, FDA advisers back gene therapy for rare form of blindness. *Nature* **550**, 314 (2017).
906 6. B. Bakondi *et al.*, In Vivo CRISPR/Cas9 Gene Editing Corrects Retinal Dystrophy in the S334ter-3 Rat Model
907 of Autosomal Dominant Retinitis Pigmentosa. *Mol Ther* **24**, 556-563 (2016).
908 7. Y. T. Tsai *et al.*, Clustered Regularly Interspaced Short Palindromic Repeats-Based Genome Surgery for the
909 Treatment of Autosomal Dominant Retinitis Pigmentosa. *Ophthalmology* **125**, 1421-1430 (2018).
910 8. P. Li, Kleinstiver, B.P., Leon, M.Y., Prew, M.S., Navarro-Gomez, D., Greenwald, S.H., Pierce, E.A., Joung,
911 J.K., Liu, Q., Allele-Specific CRISPR-Cas9 Genome Editing of the Single-Base P23H Mutation for Rhodopsin-
912 Associated Dominant Retinitis Pigmentosa. *The CRISPR Journal* **1**, 55-64 (2018).
913 9. V. Pattanayak *et al.*, High-throughput profiling of off-target DNA cleavage reveals RNA-programmed Cas9
914 nuclease specificity. *Nat Biotechnol* **31**, 839-843 (2013).
915 10. D. G. Courtney *et al.*, CRISPR/Cas9 DNA cleavage at SNP-derived PAM enables both in vitro and in vivo
916 KRT12 mutation-specific targeting. *Gene Ther* **23**, 108-112 (2016).
917 11. M. K. Cromer *et al.*, Global Transcriptional Response to CRISPR/Cas9-AAV6-Based Genome Editing in
918 CD34(+) Hematopoietic Stem and Progenitor Cells. *Mol Ther* **26**, 2431-2442 (2018).
919 12. S. Lessard *et al.*, Human genetic variation alters CRISPR-Cas9 on- and off-targeting specificity at
920 therapeutically implicated loci. *Proc Natl Acad Sci U S A* **114**, E11257-E11266 (2017).
921 13. M. L. Maeder *et al.*, Development of a gene-editing approach to restore vision loss in Leber congenital
922 amaurosis type 10. *Nat Med* **25**, 229-233 (2019).
923 14. K. E. Guziewicz *et al.*, Bestrophinopathy: An RPE-photoreceptor interface disease. *Prog Retin Eye Res* **58**,
924 70-88 (2017).
925 15. A. A. Johnson *et al.*, Bestrophin 1 and retinal disease. *Prog Retin Eye Res* **58**, 45-69 (2017).
926 16. V. K. Dickson, L. Pedi, S. B. Long, Structure and insights into the function of a Ca2+-activated Cl- channel.
927 *Nature* **516**, 213-218 (2014).
928 17. R. Singh *et al.*, iPS cell modeling of Best disease: insights into the pathophysiology of an inherited macular
929 degeneration. *Hum Mol Genet* **22**, 593-607 (2013).
930 18. R. Singh *et al.*, Pharmacological Modulation of Photoreceptor Outer Segment Degradation in a Human iPS
931 Cell Model of Inherited Macular Degeneration. *Mol Ther* **23**, 1700-1711 (2015).
932 19. B. Steyer *et al.*, Scarless Genome Editing of Human Pluripotent Stem Cells via Transient Puromycin
933 Selection. *Stem Cell Reports* **10**, 642-654 (2018).
934 20. A. Milenkovic, V. M. Milenkovic, C. H. Wetzel, B. H. F. Weber, BEST1 protein stability and degradation
935 pathways differ between autosomal dominant Best disease and autosomal recessive bestrophinopathy
936 accounting for the distinct retinal phenotypes. *Hum Mol Genet* **27**, 1630-1641 (2018).
937 21. A. D. Marmorstein *et al.*, Mutant Best1 Expression and Impaired Phagocytosis in an iPSC Model of
938 Autosomal Recessive Bestrophinopathy. *Sci Rep* **8**, 4487 (2018).
939 22. K. E. Guziewicz *et al.*, BEST1 gene therapy corrects a diffuse retina-wide microdetachment modulated by
940 light exposure. *P Natl Acad Sci USA* **115**, E2839-E2848 (2018).

bioRxiv preprint doi: https://doi.org/10.1101/796581; this version posted January 30, 2020. The copyright holder for this preprint (which was not certified by peer review) is the author/funder, who has granted bioRxiv a license to display the preprint in perpetuity. It is made available under aCC-BY-NC 4.0 International license.

941 23. Y. Li *et al.*, Patient-specific mutations impair BESTROPHIN1's essential role in mediating Ca(2+)-dependent
942 Cl(-) currents in human RPE. *Elife* **6** (2017).
943 24. N. Waugh *et al.*, Treatments for dry age-related macular degeneration and Stargardt disease: a systematic
944 review. *Health Technol Assess* **22**, 1-168 (2018).
945 25. P. K. Shahi *et al.*, Gene Augmentation and Readthrough Rescue Channelopathy in an iPSC-RPE Model of
946 Congenital Blindness. *Am J Hum Genet* **104**, 310-318 (2019).
947 26. D. B. Cox, R. J. Platt, F. Zhang, Therapeutic genome editing: prospects and challenges. *Nat Med* **21**, 121-
948 131 (2015).
949 27. M. W. Popp, L. E. Maquat, Leveraging Rules of Nonsense-Mediated mRNA Decay for Genome Engineering
950 and Personalized Medicine. *Cell* **165**, 1319-1322 (2016).
951 28. R. G. H. Lindeboom, M. Vermeulen, B. Lehner, F. Supek, The impact of nonsense-mediated mRNA decay
952 on genetic disease, gene editing and cancer immunotherapy. *Nat Genet* **51**, 1645-1651 (2019).
953 29. M. Sadelain, E. P. Papapetrou, F. D. Bushman, Safe harbours for the integration of new DNA in the human
954 genome. *Nat Rev Cancer* **12**, 51-58 (2011).
955 30. M. W. Shen *et al.*, Predictable and precise template-free CRISPR editing of pathogenic variants. *Nature*
956 **563**, 646-651 (2018).
957 31. C. J. Boon *et al.*, The spectrum of ocular phenotypes caused by mutations in the BEST1 gene. *Prog Retin*
958 *Eye Res* **28**, 187-205 (2009).
959 32. C. Ji *et al.*, Investigation and Restoration of BEST1 Activity in Patient-derived RPEs with Dominant
960 Mutations. *Sci Rep* **9**, 19026 (2019).
961 33. A. A. Johnson *et al.*, Disease-causing mutations associated with four bestrophinopathies exhibit disparate
962 effects on the localization, but not the oligomerization, of Bestrophin-1. *Exp Eye Res* **121**, 74-85 (2014).
963 34. V. Vasireddy *et al.*, AAV-mediated gene therapy for choroideremia: preclinical studies in personalized
964 models. *PLoS One* **8**, e61396 (2013).
965 35. G. Vaisey, A. N. Miller, S. B. Long, Distinct regions that control ion selectivity and calcium-dependent
966 activation in the bestrophin ion channel. *Proc Natl Acad Sci U S A* **113**, E7399-E7408 (2016).
967 36. A. V. Cideciyan *et al.*, Mutation-independent rhodopsin gene therapy by knockdown and replacement
968 with a single AAV vector. *Proc Natl Acad Sci U S A* **115**, E8547-E8556 (2018).
969 37. P. Mali *et al.*, RNA-guided human genome engineering via Cas9. *Science* **339**, 823-826 (2013).
970 38. B. Wienert, J. Shin, E. Zelin, K. Pestal, J. E. Corn, In vitro-transcribed guide RNAs trigger an innate immune
971 response via the RIG-I pathway. *PLoS Biol* **16**, e2005840 (2018).
972 39. A. L. George, Jr., Inherited Channelopathies Associated with Epilepsy. *Epilepsy Curr* **4**, 65-70 (2004).
973 40. C. P. Schaaf, Nicotinic acetylcholine receptors in human genetic disease. *Genet Med* **16**, 649-656 (2014).
974 41. C. Villa, R. Combi, Potassium Channels and Human Epileptic Phenotypes: An Updated Overview. *Front Cell*
975 *Neurosci* **10**, 81 (2016).
976 42. R. Singh *et al.*, Functional analysis of serially expanded human iPS cell-derived RPE cultures. *Invest*
977 *Ophthalmol Vis Sci* **54**, 6767-6778 (2013).
978 43. A. Kuruma, H. C. Hartzell, Bimodal control of a Ca(2+)-activated Cl(-) channel by different Ca(2+) signals. *J*
979 *Gen Physiol* **115**, 59-80 (2000).
980 44. L. Pinello *et al.*, Analyzing CRISPR genome-editing experiments with CRISPResso. *Nat Biotechnol* **34**, 695-
981 697 (2016).
982 45. N. V. Strunnikova *et al.*, Transcriptome analysis and molecular signature of human retinal pigment
983 epithelium. *Hum Mol Genet* **19**, 2468-2486 (2010).
984 46. D. D. Lee, H. S. Seung, Algorithms for Non-negative Matrix Factorization. *Advances in Neural Information*
985 *Processing Systems* **13**, 556-562 (2000).
986 47. J. G. Doench *et al.*, Optimized sgRNA design to maximize activity and minimize off-target effects of
987 CRISPR-Cas9. *Nat Biotechnol* **34**, 184-191 (2016).

bioRxiv preprint doi: https://doi.org/10.1101/796581; this version posted January 30, 2020. The copyright holder for this preprint (which was not certified by peer review) is the author/funder, who has granted bioRxiv a license to display the preprint in perpetuity. It is made available under aCC-BY-NC 4.0 International license.

988 48. P. D. Hsu *et al.*, DNA targeting specificity of RNA-guided Cas9 nucleases. *Nat Biotechnol* **31**, 827-832
989 (2013).
990